



HAL
open science

Application of the Multi-Scale Infrastructure for Chemistry and Aerosols version 0 (MUSICAv0) for air quality in Africa

Wenfu Tang, Louisa K Emmons, Helen Worden, Rajesh Kumar, Cenlin He, Benjamin Gaubert, Zhonghua Zheng, Simone Tilmes, Rebecca R Buchholz, Sara-Eva Martinez-Alonso, et al.

► **To cite this version:**

Wenfu Tang, Louisa K Emmons, Helen Worden, Rajesh Kumar, Cenlin He, et al.. Application of the Multi-Scale Infrastructure for Chemistry and Aerosols version 0 (MUSICAv0) for air quality in Africa. *Geoscientific Model Development*, 2023, 16 (13), pp.3873-3891. 10.5194/gmd-2023-50 . hal-04235272

HAL Id: hal-04235272

<https://cnrs.hal.science/hal-04235272>

Submitted on 10 Oct 2023

HAL is a multi-disciplinary open access archive for the deposit and dissemination of scientific research documents, whether they are published or not. The documents may come from teaching and research institutions in France or abroad, or from public or private research centers.

L'archive ouverte pluridisciplinaire **HAL**, est destinée au dépôt et à la diffusion de documents scientifiques de niveau recherche, publiés ou non, émanant des établissements d'enseignement et de recherche français ou étrangers, des laboratoires publics ou privés.



1 **Application of the Multi-Scale Infrastructure for Chemistry and Aerosols**
2 **version 0 (MUSICAv0) for air quality in Africa**

3
4
5 **Wenfu Tang¹, Louisa K. Emmons¹, Helen M. Worden¹, Rajesh Kumar², Cenlin He²,**
6 **Benjamin Gaubert¹, Zhonghua Zheng³, Simone Tilmes¹, Rebecca R. Buchholz¹, Sara-Eva**
7 **Martinez-Alonso¹, Claire Granier^{4,5}, Antonin Soulie⁴, Kathryn McKain^{5,6}, Bruce C. Daube⁷,**
8 **Jeff Peischl^{5,8}, Chelsea Thompson⁸, and Pieter Levelt^{1,9,10}**

9
10 ¹Atmospheric Chemistry Observations & Modeling Laboratory, National Center for Atmospheric
11 Research, Boulder, CO, USA

12 ²Research Applications Laboratory, National Center for Atmospheric Research, Boulder, CO,
13 USA

14 ³Department of Earth and Environmental Sciences, The University of Manchester, Manchester
15 M13 9PL, United Kingdom

16 ⁴Laboratoire d'Aérodynamique, CNRS, Université de Toulouse, Toulouse, France

17 ⁵Cooperative Institute for Research in Environmental Sciences (CIRES), University of Colorado,
18 Boulder, CO, USA

19 ⁶Global Monitoring Laboratory (GML), National Oceanic and Atmospheric Administration,
20 Boulder, CO, USA

21 ⁷Department of Earth and Planetary Sciences, Harvard University, Cambridge, MA, USA

22 ⁸NOAA Chemical Sciences Laboratory, Boulder, CO, USA

23 ⁹Royal Netherlands Meteorological Institute (KNMI), Utrechtseweg 297, 3730 AE De Bilt, the
24 Netherlands

25 ¹⁰University of Technology Delft, Mekelweg 5, 2628 CD Delft, the Netherlands

26
27 Correspondence: Wenfu Tang (wenfut@ucar.edu)

28
29
30 **Abstract**

31 The Multi-Scale Infrastructure for Chemistry and Aerosols Version 0 (MUSICAv0) is a new
32 community modeling infrastructure that enables the study of atmospheric composition and
33 chemistry across all relevant scales. We develop a MUSICAv0 grid with Africa refinement (~28
34 km × 28 km over Africa). We evaluate the MUSICAv0 simulation for 2017 with in situ
35 observations and compare the model results to satellite products over Africa. A simulation from
36 the Weather Research and Forecasting model coupled with Chemistry (WRF-Chem), a regional
37 model that is widely used in Africa studies, is also included in the analyses as a reference. Overall,
38 the performance of MUSICAv0 is comparable to WRF-Chem. Both models underestimate carbon
39 monoxide (CO) compared to in situ observations and satellite CO column retrievals from the
40 Measurements of Pollution in the Troposphere (MOPITT) satellite instrument. MUSICAv0 tends
41 to overestimate ozone (O₃), likely due to overestimated stratosphere-to-troposphere flux of ozone.
42 Both models significantly underestimate fine particulate matter (PM_{2.5}) at two surface sites in East
43 Africa. The MUSICAv0 simulation agrees better with aerosol optical depth (AOD) retrievals from
44 the Moderate Resolution Imaging Spectroradiometer (MODIS) and tropospheric nitrogen dioxide



45 (NO₂) column retrievals from the Ozone Monitoring Instrument (OMI) than WRF-Chem.
46 MUSICA_{v0} has a consistently lower tropospheric formaldehyde (HCHO) column than OMI
47 retrievals. Based on model-satellite discrepancies between MUSICA_{v0} and WRF-Chem and
48 MOPITT CO, MODIS AOD, and OMI tropospheric NO₂, we find that future field campaign(s)
49 and more in situ observations in an East African region (30°E – 45°E, 5°S – 5°N) could
50 substantially improve the predictive skill of atmospheric chemistry model(s). This suggested focus
51 region exhibits the largest model-in situ observation discrepancies, as well as targets for high
52 population density, land cover variability, and anthropogenic pollution sources.

53

54 1. Introduction

55 As one of the most dramatically changing continents, Africa is experiencing myriad
56 environmental sustainability issues (e.g., Washington et al., 2006; Ziervogel et al., 2014; Boone
57 et al., 2016; Baudoin et al., 2017; Güneralp et al., 2017; Nicholson 2019; Fisher et al., 2021; Kumar
58 et al., 2022). These environmental issues are causing vast losses in lives and in African economies,
59 and are coupled with poverty and under-development (Washington et al., 2006; Fisher et al., 2021).
60 Some of these environmental challenges are particularly severe in Africa compared to many other
61 regions of the world (e.g., famine, droughts, floods, high temperatures, land degradation, and fires;
62 Washington et al., 2006; van der Werf et al., 2017). However, even though Africa is the second
63 largest continent, in land area and population, attention and research on environmental challenges
64 in Africa are very limited, leading to a deficit of knowledge and solutions (e.g., De Longueville et
65 al., 2010). Degraded air quality is an example of a severe environmental challenge with growing
66 importance in Africa (e.g., Liousse et al., 2014; Thompson et al., 2014; Heft-Neal et al., 2018;
67 Fisher et al., 2021; Vohra et al., 2022). A previous study found that air pollution across Africa
68 caused ~1.1 million deaths in 2019 (Fisher et al., 2021). However, the study of air quality in Africa
69 is hindered by the scarcity of ground-based observations (e.g., Paton-Walsh et al., 2022),
70 modelling capability and the use of satellite observations. In this paper, we will focus on air quality
71 analyses over Africa with the new model Multi-Scale Infrastructure for Chemistry and Aerosols
72 (MUSICA; Pfister et al., 2020).

73 Atmospheric chemistry modeling is a useful tool to perform research on air quality
74 conditions and evolution. Various models have been applied to study atmospheric chemistry and
75 air quality in Africa such as the Weather Research and Forecasting (WRF) model coupled with
76 Chemistry (WRF-Chem) (e.g., Kuik et al., 2015; Kumar et al., 2022), the GEOS-Chem chemical
77 transport model (e.g., Marais et al., 2012, 2019; Lacey et al., 2018), the CHIMERE chemical
78 transport model (e.g., Menut et al., 2018; Mazzeo et al., 2022), and the U.K. Earth System Model
79 (UKESM1) (Brown et al., 2022), and GEOS5 (Bauer et al., 2019).

80 MUSICA is a new state-of-the-art community modeling infrastructure that enables the
81 study of atmospheric composition and chemistry across all relevant scales (Pfister et al., 2020).
82 The newly developed MUSICA Version 0 (MUSICA_{v0}) is a global chemistry-climate model that
83 allows global simulations with regional refinement down to a few kilometers spatial resolution
84 (Schwantes et al., 2022). The coupling with other components of the Earth system (e.g., land,
85 ocean, and sea ice) can also be performed at multiple scales. MUSICA_{v0} has various advantages
86 and is particularly suitable for research applications over Africa. For example, MUSICA_{v0} can be
87 used to study the interactions between atmospheric chemistry and other components of the Earth
88 system and climate. MUSICA also includes the whole atmosphere (from the surface to
89 thermosphere), and therefore can also be used to study the stratosphere and above and interactions
90 between the stratosphere and troposphere. This is critical because some of the environmental issues



91 in Africa are coupled (e.g., the ozone–climate penalty; Brown et al., 2022). In addition, as a global
92 model, MUSICAv0 does not require boundary conditions to study a region at high resolution.
93 Global impacts and interactions can be simulated in a consistent and coherent way. This feature is
94 important as inflow from other continents and oceans significantly impacts air quality in Africa.
95 MUSICAv0 has been evaluated over North America (Schwantes et al., 2022, Tang et al., 2022)
96 and is also being developed and tested in other regions around the globe
97 (<https://wiki.ucar.edu/display/MUSICA/Available+Grids>).

98 This paper serves as the basis for the future application of MUSICAv0 in Africa. In this
99 study, we develop a MUSICAv0 model grid with regional refinement over Africa. Because
100 MUSICAv0 with Africa refinement is newly developed while WRF-Chem has been previously
101 used for African atmospheric chemistry and air quality studies, here we include results from WRF-
102 Chem to assess the ability of MUSICAv0 in reproducing the regional features of atmospheric
103 composition as simulated by WRF-Chem. We conduct the MUSICAv0 simulation for the year
104 2017 to compare with a previous WRF-Chem simulation (Kumar et al., 2022). MUSICAv0 and
105 the WRF-Chem simulation and the observational data used in this study are described in Section
106 2. The MUSICAv0 model simulation results are evaluated against in situ observations and
107 compared with satellite retrievals in Section 3. In Section 4, we provide an example application of
108 MUSICAv0 over Africa – identifying key potential regions in Africa for future in situ observations
109 and field campaign(s).

111 2. Model and data

112 2.1 MUSICAv0

113 MUSICAv0 is a newly developed framework for simulations of large-scale atmospheric
114 phenomena in a global modeling framework, while still resolving chemistry at emission- and
115 exposure-relevant scales (Pfister et al., 2020). MUSICAv0 is a configuration
116 of the Community Earth System Model (CESM). It is also known as the Community Atmospheric
117 Model with chemistry (CAM-chem) (Tilmes et al., 2019; Emmons et al., 2020) with regional
118 refinement (RR) down to a few kilometers (Lauritzen et al., 2018; Schwantes et al., 2022). CAM-
119 chem, and thus MUSICAv0, includes several choices of chemical mechanisms of varying
120 complexity. This study uses the default MOZART-TS1 chemical mechanism for gas phase
121 chemistry (including comprehensive tropospheric and stratospheric chemistry; Emmons et al.,
122 2020) and the four-mode version of the Modal Aerosol Module (MAM4; Liu et al., 2016) for the
123 aerosol scheme.

124 The MUSICAv0 users have the option to create their own model grid. MUSICAv0 is
125 currently being developed and tested for applications over various regions globally
126 (<https://wiki.ucar.edu/display/MUSICA/Available+Grids>), including North America, India, East
127 Asia, South America, Australia, and Korea, among others. (e.g., Schwantes et al., 2022; Tang et
128 al., 2022; Jo et al., 2023). In this study, we develop a model grid for applications in Africa
129 (`ne0np4.africa_v5.ne30x4`). As shown in Figure 1a, the horizontal resolution is $\sim 111 \text{ km} \times 111 \text{ km}$
130 (i.e., 1° latitude \times 1° equatorial longitude) globally, and $\sim 28 \text{ km} \times 28 \text{ km}$ (i.e., 0.25° latitude \times
131 0.25° equatorial longitude) within the region over Africa. Our simulation uses the default option
132 for vertical layers (i.e., 32 layers from the surface to $\sim 3.64 \text{ hPa}$).

133 Here we run MUSICAv0 with the model grid for Africa for the year 2017, saving 3-hourly
134 output. We use the Copernicus Atmosphere Monitoring Service Global Anthropogenic emissions,
135 (CAM5-GLOB-ANTH) version 5.1 (Soulie et al., 2023) for anthropogenic emissions and the



136 Quick Fire Emissions Dataset (QFED) for fire emissions (Darmenov and da Silva, 2013). Plume
137 rise climatology is applied to fire emissions following Tang et al. (2022). In addition, we also
138 include open waste burning (<https://www.acom.ucar.edu/Data/fire/>; Wiedinmyer et al., 2014)
139 emissions in the simulation. The model has the option of a free-running atmosphere or nudging to
140 external meteorological reanalysis. In this simulation, only wind and temperature are nudged to
141 the Modern-Era Retrospective analysis for Research and Applications, Version 2 (MERRA-2;
142 Gelaro et al., 2017) with a relaxation time of 12 hours.

143 We also added carbon monoxide (CO) tracers in the simulation to understand the source
144 and transport of air pollution. CO tracers in CAM-chem/MUSICAv0 are described in detail by
145 Tang et al. (2019). In this study we include tracers for 6 regions (North Africa, West Africa, East
146 Africa, Central Africa, Southern Africa, and the rest of the world) and 3 emission sources
147 separately (anthropogenic emissions, fire emissions, and open waste burning emissions). In total,
148 there are 18 tagged CO tracers.

149

150 2.2 WRF-Chem

151 The Weather Research and Forecasting (WRF) model coupled with Chemistry (WRF-
152 Chem) is a regional chemical transport model. It has been widely used for air quality studies in
153 Africa. In this study we use model results from a WRF-Chem simulation described by Kumar et
154 al. (2022). The WRF-Chem simulation has a grid spacing of 20 km, slightly higher than the
155 MUSICAv0 simulation, and the model domain is highlighted in Figure 1a. The simulation has 36
156 vertical levels from the surface to ~50 hPa. The WRF-Chem simulation uses the Model for Ozone
157 and Related Tracers-4 (MOZART-4) chemical mechanism (Emmons et al., 2010) for tropospheric
158 gas phase chemistry, and the Goddard Global Ozone Chemistry Aerosol Radiation and Transport
159 (GOCART) model (Chin et al., 2002) for aerosol processes. The European Centre for Medium
160 Range Weather Forecasts (ECMWF) global reanalysis (ERA-Interim) fields are used for initial
161 and boundary meteorology conditions, while another CAM-chem simulation is used for initial
162 and boundary chemical conditions (Kumar et al., 2022). The WRF-Chem simulation used the global
163 Emission Database for Atmospheric Research developed for Hemispheric Transport of Air
164 Pollution (EDGAR-HTAP v2) for anthropogenic emissions and the Fire Inventory from NCAR
165 version 1.5 (FINNv1.5) (Wiedinmyer et al., 2011) for fire emissions. The WRF-Chem output is
166 saved hourly, however we only use 3-hourly output to match the MUSICAv0 simulation.

167

168 2.3 ATom

169 The Atmospheric Tomography mission (ATom; Thompson et al. 2022) was designed to
170 study the impact of human-produced air pollution on greenhouse gases, chemically reactive gases,
171 and aerosols in remote ocean air masses. During the project, the DC-8 aircraft sampled the remote
172 troposphere with continuous vertical profiles. There were four seasonal deployments from the
173 summer of 2016 through the spring of 2018. Here we compare the MUSICAv0 simulation with
174 observations from ATom-2 (January–February 2017) and ATom-3 (September–October 2017).
175 Since the ATom flight tracks were mostly outside the WRF-Chem domain (Figure 1a), we do not
176 compare the WRF-Chem simulation with ATom data. However, we compare chemical species
177 from the MUSICAv0 simulation to the 2-minute merged ATom measurements globally to obtain
178 a benchmark and broader understanding of MUSICAv0 performance both within and outside the
179 refined region. The model output is saved along the ATom aircraft flight tracks and with respect
180 to the observational times at run time. Nitric oxide (NO) and ozone (O₃) measurements from the
181 NOAA Nitrogen Oxides and Ozone (NOyO₃) instrument (Bourgeois et al., 2020, 2021) and the



182 merged CO data (from Quantum Cascade Laser System and NOAA Picarro CO measurements)
183 are used.

184

185 **2.4 IAGOS**

186 The In-service Aircraft for a Global Observing System (IAGOS) is a European research
187 infrastructure, and was developed for operations on commercial aircraft to monitor atmospheric
188 composition (Petzold et al., 2015). The IAGOS instrument package 1 measures CO, O₃, air
189 temperature, and water vapor (<https://www.iagos.org/iagos-core-instruments/package1/>). CO is
190 measured by infrared absorption using the gas filter correlation technique (Precision: ±5%,
191 Accuracy: ±5 ppb) while O₃ is measured by UV absorption at 253.7 nm (Precision: ±2%,
192 Accuracy: ±2 ppb). We use airborne measurements of CO, O₃, air temperature, and water vapor
193 from IAGOS for model evaluation. The locations of the IAGOS flight tracks over Africa are shown
194 in Figure 1b. The model results and IAGOS data comparisons are conducted separately for five
195 African sub-regions (defined in Figure 1b).

196

197 **2.5 Ozonesondes**

198 The ozonesonde is a balloon-borne instrument that measures atmospheric O₃ profiles
199 through the electrochemical concentration cell using iodine/iodide electrode reactions (Thompson
200 et al., 2017), with records of temperature, pressure, and relative humidity from standard
201 radiosondes. We use ozonesonde data from Southern Hemisphere ADDitional OZonesondes
202 (NASA/GSFC SHADOZ; Thompson et al., 2017; Witte et al., 2017, 2018). Specifically,
203 ozonesonde data from four sites are used (Figure 1b): Ascension (Ascension Island, U.K.), Nairobi
204 (Kenya), Irene (South Africa), and La Reunion (La Réunion Island, France). The average O₃
205 measurement uncertainty ranged from 5–9% for the ozonesonde data used in this study.

206

207 **2.6 WDCGG**

208 Monthly surface CO measurements from the World Data Center for Greenhouse Gases
209 (WDCGG; operated by the Japan Meteorological Agency in collaboration with the World
210 Meteorological Organization) are used for model evaluation. Data from six sites are used (Figure
211 1b), namely (Ascension Island, U.K.), Assekrem (Algeria; remote site located in Saharan desert),
212 Gobabeb (Namibia; located at the base of a linear sand dune, next to an interdune plain), Cape
213 Point (South Africa; site exposed to the sea on top of a cliff 230 meters above sea level), Izana
214 (Tenerife, Spain; located on the Island that is ~300 km west of the African coast), and Mare
215 (Seychelles; near an international airport).

216

217 **2.7 Surface PM_{2.5}**

218 At the U.S. embassies, regulatory-grade monitoring data are collected with Beta
219 Attenuation Monitors (BAMs), using a federal equivalent monitoring method, with an accuracy
220 within 10% of federal reference methods (Watson et al., 1998; U.S. EPA, 2016). These instruments
221 are operated by the U.S. State Department and the U.S. EPA, and data are available through
222 AirNow (<https://www.airnow.gov/international/us-embassies-and-consulates/>). We use the
223 measurements at the U.S. embassy locations in Addis Ababa Central (Ethiopia, 9.06° N, 38.76° E)
224 and Kampala (Uganda, 0.30° N, 32.59° E) for the year 2017 as references (Malings et al., 2020)
225 to match our simulations. The raw data are made available hourly and for this study we use daily
226 mean PM_{2.5} for comparison with model simulations.

227



228 **2.8 MOPITT**

229 The Measurements of Pollution in the Troposphere (MOPITT) instrument on board the
230 NASA Terra satellite provides both thermal-infrared (TIR) and near-infrared (NIR) radiance
231 measurements since March 2000. Retrievals of CO column density and vertical profiles are
232 provided in a multispectral TIR–NIR joint product which has sensitivity to near-surface as well as
233 free tropospheric CO (Deeter et al., 2011; Worden et al., 2010). Here we use the MOPITT Version
234 9 Level 2 CO column product (Deeter et al., 2022) over Africa to evaluate the MUSICAv0 and
235 WRF-Chem simulations. MOPITT Version 9 has significant updates to the cloud detection
236 algorithm and NIR calibration scheme. The MOPITT satellite pixel size is $\sim 22 \text{ km} \times 22 \text{ km}$, and
237 the overpass time is $\sim 10:30$ am local time in 2017. When comparing model outputs to MOPITT
238 the recommended data quality filter is applied and model outputs are interpolated to the MOPITT
239 retrievals in space and time. To perform quantitative comparisons, the MOPITT averaging kernel
240 and a priori are used to transform the model CO profiles to derive model column amounts.

241

242 **2.9 OMI NO₂ (QA4ECV)**

243 Tropospheric column NO₂ from the Ozone Monitoring Instrument (OMI) on board Aura
244 is compared to the model in this study. Specifically, the NO₂ product from the quality assurance
245 for the essential climate variables (QA4ECV) project is used (Boersma et al., 2017a; Compornelle
246 et al., 2020). The satellite pixel size is $\sim 13 \text{ km} \times 25 \text{ km}$, and the overpass time is $\sim 1:40$ pm local
247 time in 2017. A data quality filter was applied following the Product Specification Document
248 (Boersma et al., 2017b; `processing_error_flag = 0`, `solar_zenith_angle < 80`, `snow_ice_flag < 10`
249 or `snow_ice_flag = 255`, `amf_trop/amf_geo > 0.2`, and `cloud_radiance_fraction_no20 <= 0.5`).
250 Model profiles were transformed using the provided tropospheric air mass factor (AMF) and
251 averaging kernels.

252

253 **2.10 OMI HCHO (QA4ECV)**

254 We also use tropospheric column HCHO from OMI in this study. Similar to OMI NO₂, we
255 also use OMI HCHO product from QA4ECV (De Smedt et al., 2017a). A data quality filter was
256 applied following the Product User Guide (De Smedt et al., 2017b; `processing_error_flag = 0` and
257 `processing_quality_flag = 0`). Model profiles were transformed using provided averaging kernels.
258 We note that HCHO retrievals are subject to relatively large uncertainties compared to other
259 satellite products used in this study. Therefore, the comparisons between model results and the
260 OMI HCHO product only indicate the model-satellite discrepancies rather than determining model
261 deficiencies. In addition, the WRF-Chem simulation from Kumar et al. (2022) does not include
262 HCHO in the output and hence will not be compared.

263

264 **2.11 MODIS AOD**

265 The aerosol optical depth (AOD) product (550 nm) from the Moderate Resolution Imaging
266 Spectroradiometer (MODIS) on board Terra NASA Terra satellite is used. Specifically, we used
267 the MODIS Level 2 Collection 6.1 product (MOD04_L2; Levy et al., 2017). Deep Blue Aerosol
268 retrievals are used (Hsu et al., 2013; Levy et al., 2013) to include retrievals over the desert. The
269 MODIS satellite pixel size is $\sim 1 \text{ km} \times 1 \text{ km}$, and the overpass time is $\sim 10:30$ am local time.

270

271 **3. Model comparisons with satellite data and evaluation with in situ observations**

272 Africa includes a wide range of environments and emissions source. Therefore, in this
273 section we separate the continent in five sub-regions for analysis following Kumar et al. (2022).



274 CO is a good tracer of anthropogenic and biomass burning emissions and modeled CO tracers are
275 used in this section to understand sources. Figure 2 shows the seasonal averages of CO column
276 distributions over Africa from MOPITT along with the MUSICAv0 and WRF-Chem biases. The
277 highest levels of CO in these maps are primarily associated with biomass burning, which moves
278 around the continent with season. Both MUSICAv0 and WRF-Chem simulations underestimate
279 the CO column compared to MOPITT (Figures 3a and 3b). Overall, MUSICAv0 agrees better with
280 the OMI tropospheric NO₂ column (Figure 3c) and MODIS AOD (Figure 3e) than WRF-Chem
281 (Figures 3d and 3f). The MUSICAv0 simulation overall has lower tropospheric HCHO column
282 than OMI in all regions and seasons (Figure 3g). Spatial distributions of model biases against the
283 OMI tropospheric NO₂ column, MODIS AOD, and OMI tropospheric HCHO column are included
284 in Figures S1–S3. In this section we compare the model results with satellite data and in situ
285 observations over sub-regions in Africa and oceans near Africa (Figure 1b).

286 287 **3.1 North Africa**

288 Over North Africa, both MUSICAv0 and WRF-Chem simulations underestimate the CO
289 column during 2017 (Figures 2 and 3). As shown by the tagged model CO tracers (Figure 4), CO
290 over North Africa is mainly driven by transport of CO from outside the continent and
291 anthropogenic emissions. The model underestimation compared to the MOPITT CO column is
292 consistent with the results of the comparisons with surface CO observations from WDCGG at the
293 two sites located in North Africa (Assekrem and Izana; Figures 5a and 5c). At the two surface
294 sites, the composition of source types and source regions are close to the composition of source
295 types and source regions of the column average over North Africa (Figure 4 and Figures S4 and
296 S5), hence the two sites are representative of the background conditions of North Africa.
297 Compared to MODIS AOD, WRF-Chem has a mean bias of 0.36 whereas MUSICAv0's mean
298 bias is 0.17 for 2017. The model AOD biases over North Africa are likely driven by dust. No
299 comparison is made with IAGOS O₃ in North Africa due to data availability.

300 301 **3.2 West Africa**

302 Over West Africa, fire and anthropogenic emissions are both important for CO pollutant
303 and fire impacts peak in DJF (December, January, and February). Compared to the MOPITT CO
304 column, the mean bias of MUSICAv0 and WRF-Chem for West Africa peak around February –
305 the dry season of the Northern Hemisphere (Figure 3). In February, the MUSICAv0 mean bias is
306 -1.1×10^{18} molecules/cm² and WRF-Chem mean bias is -7.5×10^{17} molecules/cm², which are likely
307 driven by fire emission sources (Figure 4). Model comparisons with IAGOS CO also show a
308 similar bias – both model simulations underestimate CO at all vertical levels. The underestimation
309 peaks during DJF and below 600 hPa (Figure 6). As for MODIS AOD, WRF-Chem has the mean
310 bias 0.69 whereas MUSICAv0's mean bias is 0.15, respectively. Similar to North Africa, the model
311 biases in AOD over West Africa are also likely driven by dust and biomass burning. We also
312 compare modeled O₃ with IAGOS O₃ observations (Figure 7).

313 Over West Africa, both models agree well with the IAGOS O₃ observations below 800 hPa
314 (mean bias ranges from -1 to -4 ppb). Above 800 hPa over West Africa, WRF-Chem
315 underestimates O₃ while MUSICAv0 overestimates O₃. Overall, MUSICAv0 consistently
316 overestimates O₃ above 800 hPa in all seasons while the direction of WRF-Chem bias changes
317 with seasons (Figure 7). When MUSICAv0 overestimates O₃, the bias is in general larger at the
318 higher altitude of the troposphere. The concentration of the model stratospheric ozone tracer, O3S,
319 is also larger at the higher altitude in DJF (Figure 9). The correlation of modeled O₃ and O3S is



0.54, and the correlations of O₃S and model O₃ bias (modeled O₃ minus IAGOS O₃) is 0.35 over West Africa, implying the overestimation of O₃ in the upper troposphere could be partially driven by too strong stratosphere-to-troposphere flux of ozone. Lightning NO emissions can also impact O₃ in the upper troposphere. The MUSICAv0 simulation has somewhat (~3 times) higher lightning NO emissions (Figure S6) compared to a standard CAM-chem simulation (not shown), therefore the high ozone in the upper troposphere may be due to an over-estimate of lightning NO. Impacts of lightning NO emissions on upper troposphere O₃ in MUSICAv0 will be investigated and evaluated further in the future. A brief comparison with IAGOS measurements of air temperature and water vapor profiles over West Africa as well as other sub-regions shows that MUSICAv0 overall agrees well with these meteorological variables (Figure S7).

330

331

3.3 Central Africa

332

333

334

335

336

337

338

339

340

341

342

343

344

345

346

347

348

349

350

351

352

353

354

355

356

357

358

359

360

361

362

363

364

365

Compared to MOPITT CO column, the mean bias of MUSICAv0 and WRF-Chem for Central Africa varies with seasons (Figure 3) but peaks during the dry season in September (MUSICAv0 mean bias of -1.0×10^{18} molecules/cm²; WRF-Chem mean bias of -1.2×10^{18} molecules/cm²). The tagged model CO tracers show that in September, local fire emissions are the dominant driver of CO in Central Africa (Figure 4). Compared to the IAGOS CO profiles (Figure 6), both models have the largest bias over Central Africa among the sub-regions in Africa – mean bias of MUSICAv0 and WRF-Chem are -46 ppb and -36 ppb, respectively. The high bias over Central Africa mainly occurs during the fire season. In central Africa, both models also underestimate NO₂ (mean biases of MUSICAv0 and WRF-Chem are -1.5×10^{14} and -5.5×10^{14} molecules/cm², respectively). The underestimations in both CO and NO₂ by the two model simulations are likely driven by the underestimation in fire emissions. Indeed, the emission estimates from the newest version of FINN (FINNv2.5; Wiedinmyer et al., 2023) are higher compared to both QFED (used in the MUSICAv0 simulation) and FINNv1.5 (used in the WRF-Chem simulation) in this region.

Model mean bias of HCHO (-1.3×10^{16} molecules/cm² for the whole 2017) over Central Africa is the largest among the five regions (Figure 3). The spatial distribution of HCHO bias (Figure S4) largely co-locates with the vegetation (Figure 8). Over the barren or sparsely vegetated area in North Africa and along the west coast of Southern Africa, HCHO biases are relatively small while over the vegetated area HCHO bias are relatively large. Over North Africa, the mean bias is -0.66×10^{16} molecules/cm² for the whole 2017 whereas over the other four regions, the mean bias ranges from -0.93×10^{16} molecules/cm² to -1.31×10^{16} molecules/cm² for the whole 2017. This indicates that the negative bias in MUSICAv0 HCHO could be due to underestimated biogenic emissions in the model. In addition, the underestimation of HCHO in Central Africa (Figure S4) co-locates with the underestimation of CO during fire season (Figure S1), implying that fire emissions may also contribute to the HCHO underestimation in MUSICAv0. It is important to note that the uncertainty of OMI tropospheric HCHO column is relatively large compared to other satellite products. Here the averaged retrieval uncertainty (random and systematic) is ~120%.

When compared to the IAGOS O₃ profiles over Central Africa (Figure 7), both models agree well with the IAGOS O₃ observations below 800 hPa (mean bias ranges from -1 to -4 ppb). Above 800 hPa, WRF-Chem underestimates O₃ while MUSICAv0 overestimates O₃. The correlation of modeled O₃ and O₃S is 0.67, and the correlations of O₃S and model O₃ bias is 0.50 over Central Africa, indicating O₃ overestimation in Central Africa are more likely to be impacted by stratosphere-to-troposphere flux of ozone than that in West Africa.



366 3.4 East Africa

367 CO over East Africa is dominated by local emissions and inflow from outside the continent.
368 Fire and anthropogenic emissions contribute approximately the same to CO over East Africa
369 (Figure 4). Both MUSICAv0 and WRF-Chem simulations underestimate the CO column
370 compared to MOPITT (Figure 3), and the WRF-Chem simulation also underestimate the
371 tropospheric NO₂ column compared to OMI. The biases in CO column and tropospheric NO₂
372 column peak in September, likely driven by fire emissions (Figure 4).

373 Compared to IAGOS O₃ profiles over East Africa, biases of MUSICAv0 below 600 hPa
374 has a seasonal variation while over 600 hPa are consistently positive (Figure 7). The correlations
375 of O₃S and model O₃ bias against IAGOS data is 0.50 in the region. The correlations between O₃S
376 and model O₃ bias are highest over Central and East Africa compared to other regions, indicating
377 stratosphere influence are strongest in these two regions among the sub-regions. Central and East
378 Africa are relatively more mountainous therefore topography driven stratospheric intrusions might
379 be expected. The Nairobi ozonesonde site is located in East Africa (Figure 1b). When comparing
380 to the O₃ profiles from ozonesondes (Figure 9), MUSICAv0 overall overestimates O₃ in the
381 troposphere at the four sites while WRF-Chem tends to underestimate O₃ in the free troposphere
382 (below 200 hPa). The Nairobi site is an exception where both MUSICAv0 and WRF-Chem
383 simulations significantly overestimate O₃ in all seasons (mean bias of MUSICAv0 and WRF-
384 Chem below 200 hPa are 27 ppb and 20 ppb, respectively). Among the four ozonesonde sites,
385 correlations of model bias of O₃ and O₃S are highest at the Nairobi site (0.74) where the model
386 significantly overestimates O₃. The results of model-ozonesonde comparisons are consistent with
387 the results of model-IAGOS comparisons and indicate a potential issue in modeled stratosphere-
388 to-troposphere flux of ozone.

389 There are two surface PM_{2.5} sites in East Africa (Addis Ababa and Kampala; Figure 1b).
390 Despite using different aerosol methods and emission inventories, both MUSICAv0 and WRF-
391 Chem underestimate surface PM_{2.5} when compared to observations at the two sites (Figure 10).
392 The errors in PM_{2.5} concentrations at the U.S. Embassy in Kampala are especially prominent.
393 However, both models approximate the variation of the PM_{2.5} in both locations. Many factors
394 contribute to the inconsistency in the magnitude of modeled PM_{2.5} concentrations. For instance,
395 emission inventories in this region require additional improvement. In Uganda, increasing motor
396 vehicle ownership and burning biomass for domestic energy use contribute to ambient PM_{2.5} levels
397 (Clarke et al., 2022; Petkova et al., 2013). Detailed PM_{2.5} composition measurements would also
398 help to pinpoint the cause of inaccuracies. In addition, model resolutions could also be a potential
399 reason for the underestimation.

400

401 3.5 Southern Africa

402 Among the five regions, MUSICAv0 has the lowest mean bias (-3.2×10^{17} molecules/cm²
403 annually) over Southern Africa (Figure 3). WRF-Chem also has low mean bias and RMSE over
404 Southern Africa except for the months of September, October, and November (SON) period where
405 WRF-Chem has larger CO mean bias (-6.2×10^{17} molecules/cm²) than MUSICAv0. Tagged model
406 CO tracers indicate that CO over Southern Africa is significantly impacted by CO emissions from
407 Central Africa, East Africa, Southern Africa, and inflow from outside the continent. As for the
408 source types, anthropogenic and fire emissions are both important and fire impacts peak in
409 September. There are two WDCGG sites located in Southern Africa (Figure 1b; Gobabeb and Cape
410 Point). When compared to surface CO observations from WDCGG, both models consistently
411 underestimate CO by up to 40% at most sites. The Cape Point site in Southern Africa is an



412 exception (Figure 5) where MUSICAv0 overestimates CO by 40 ppb (annual mean; and up to 78
413 ppb in May 2017). CO tracers in the model (Figures S4 and S5) show that CO at Cape Point is
414 mainly driven by anthropogenic CO emissions from Southern Africa. Therefore, the
415 overestimation of CO by MUSICAv0 should be due to the overestimation of anthropogenic
416 emissions from Southern Africa used in the model. As for NO₂, WRF-Chem underestimates
417 tropospheric NO₂ column in most regions except for Southern Africa (Figure 3). Over Southern
418 Africa, WRF-Chem overestimates NO₂ especially during June, July, and August (JJA).
419 MUSICAv0 also tends to overestimates NO₂ at the same location in JJA however the bias is not
420 as large as for WRF-Chem.

421 MUSICAv0 simulation overall has a lower mean bias (0.14 annually) than the WRF-Chem
422 simulation (mean bias of 0.31 annually) compared to MODIS AOD with Southern Africa being
423 the only exception (Figure 3). Over Southern Africa, MUSICAv0 overestimates AOD by ~0.21
424 annually (Figure 3) and the bias peaks in January (mean bias=0.45). This overestimation in AOD
425 over Southern Africa is not seen in WRF-Chem. It is likely that the MUSICAv0 overestimation in
426 AOD over Southern Africa is also due to biases in modeled dust as the AOD bias is co-located
427 with the only barren or sparsely vegetated area in Southern Africa (Figure 8 and Figure S3).

428 Over Southern Africa, MUSICAv0 tends to overestimate O₃ compared to IAGOS at all
429 levels at all seasons in 2017 (Figure 7). The concentration of O₃S over Southern Africa is higher
430 than those over other regions. However, the correlation of O₃S and model O₃ bias is lower than
431 other regions (0.13) indicating stratosphere-to-troposphere flux of ozone may not be the main
432 driver of O₃ bias over Southern Africa even though stratosphere-to-troposphere flux of ozone are
433 relatively strong in the region. The Irene ozonesonde site is located in Southern Africa (Figure 1b).
434 Compared to the ozonesonde O₃ profiles at the Irene site, however, the MUSICAv0 performance
435 has a seasonal variation (Figure 9e-9h). Compared to other ozonesonde sites, the correlation of
436 O₃S and model O₃ bias over Southern Africa is lower (0.14) and MUSICAv0 agrees relatively well
437 with observations, which is consistent with the comparison results with IAGOS data (Figure 7).

438

439 **3.6 Oceans near Africa**

440 We compare the CO, NO, and O₃ from the MUSICAv0 simulation with measurements
441 from ATom-2 and ATom-3 in 2017 (Figure 1a) to provide a global benchmark. Measurements
442 made over the Atlantic Ocean and Pacific Ocean, and in January-February (Jan-Feb) and
443 September-October (Sep-Oct) are compared separately (Figures 11 and 12). The comparison was
444 made with data averaged into 10° latitude and 200 hPa bins. Overall, the model consistently
445 underestimates CO globally in both seasons. The underestimation of CO is a common issue in
446 atmospheric chemistry models and could be due to various reasons, including emissions,
447 deposition, and chemistry (e.g., Fisher et al., 2017; Shindell et al., 2006; Stein et al., 2014; Tilmes
448 et al., 2015; Tang et al., 2018; Gaubert et al., 2020). Specifically for our MUSICAv0 simulation
449 in this study, the model bias in CO is relatively large (up to 52 ppb) over the Northern Hemisphere
450 (especially at high latitude and near the surface) and small over the Southern Hemisphere (Figures
451 11 and 12). Over the Atlantic Ocean, the bias in CO is larger in September-October than Jan-Feb
452 in both the Northern Hemisphere (-30 ppb in Jan-Feb versus -34 ppb in Sep-Oct) and Southern
453 Hemisphere (-11 ppb in Jan-Feb versus -14 ppb in Sep-Oct). Over the Pacific Ocean, however, the
454 CO bias is similar for both time periods in the Northern Hemisphere (-30 ppb) while in the
455 Southern Hemisphere, the CO bias changes significantly from -8 ppb in Jan-Feb to -16 ppb in Sep-
456 Oct. The changes in CO bias over the Southern Hemisphere are likely due to seasonal change in
457 fire emissions. Overall, the mean biases (Figures 11 and 12) suggest that the simulation agrees



458 better with ATom observations in the Southern Hemisphere than in the Northern Hemisphere, and
459 in Jan-Feb than in Sep-Oct (Figures 11 and 12), consistent with Gaubert et al. (2016).

460 In both seasons and both hemispheres, the model in general overestimates O₃ in the
461 stratosphere/UTLS (upper troposphere and lower stratosphere) by up to 38 ppb (above 200 hPa).
462 In the troposphere (below 200 hPa), the model overall agrees well with the ATom data over the
463 Pacific Ocean in the Southern Hemisphere (in most cases the bias is less than ±5 ppb). However,
464 over the Atlantic Ocean in the Southern Hemisphere, MUSICAv0 tends to overestimate O₃,
465 especially in Jan-Feb. In the troposphere of the Northern Hemisphere, MUSICAv0 consistently
466 overestimates O₃ over both oceans and both seasons. The positive bias in O₃ decreases from the
467 upper troposphere towards the surface, indicating that the overestimation of O₃ in the troposphere
468 may be due to stratosphere-to-troposphere flux of ozone. This was also noted for other global
469 models (Bourgeois et al. 2021). As for NO, the model tends to overestimate NO above 200 hPa
470 (approximately the stratosphere and Upper Troposphere-Lower Stratosphere; UTLS) by up to 50
471 ppt. Overall, the NO biases can be either positive or negative depending on location and season.
472 The distributions of NO bias (Figures 11 and 12) do not show an overall spatial pattern, unlike
473 those for CO (which changes monotonically with latitude) or O₃ (which changes monotonically
474 with altitude).
475

476 **4. Model application: identifying key regions in Africa for future in situ observations and** 477 **field campaign(s)**

478 As a demonstration of the application of MUSICAv0, here we use the results of model-
479 satellite comparisons to identify potential regions where the atmospheric chemistry models need
480 to be improved substantially. More field campaigns and more in situ observations would not only
481 provide observational benchmark dataset to understand and improve the modeling capability in
482 the region, but would be also useful for the validation and calibration of satellite products. Here
483 we use Taylor score to quantify model-satellite discrepancies. Taylor score (Taylor, 2001) is
484 defined by

$$485 \quad S = \frac{4(1+R)}{(\hat{\sigma}_f + 1/\sigma_f)^2(1+R_0)}$$

486 where $\hat{\sigma}_f$ is the ratio of σ_f (standard deviation of the model) and σ_r (standard deviation of
487 observations), R is correlation between model and observations, and R_0 is the maximum
488 potentially realizable correlation (=1 in this study). Taylor score ranges from 0 to 1 and a higher
489 Taylor score indicates better satellite-model agreement. To identify potential locations, we
490 separate the Africa continent into $5^\circ \times 5^\circ$ (latitude \times longitude) pixels as shown in Figure 13. And
491 for each pixel, we calculate Taylor scores of MUSICAv0 compared to the three satellite Level 2
492 products (e.g., MOPITT CO column retrievals, OMI tropospheric NO₂ column retrievals, and
493 MODIS AOD) separately. And then three Taylor scores are summed up to obtain the total Taylor
494 score for MUSICAv0 (ranges from 0 to 3) as shown in Figures 13a-13e. A similar calculation is
495 conducted for WRF-Chem (Figures 13f-13j). Note that we did not include Taylor scores for HCHO
496 in the total Taylor score due to that (1) WRF-Chem simulations did not save HCHO output, and
497 (2) the HCHO retrievals have relatively high uncertainties (Taylor scores of MUSICAv0 compared
498 to OMI tropospheric HCHO column retrievals are provided separately in Figure S8).

499 Overall, both MUSICAv0 and WRF-Chem have low total Taylor scores in the $30^\circ\text{E} - 45^\circ\text{E}$,
500 $5^\circ\text{S} - 5^\circ\text{N}$ region in East Africa (a region of 15° longitude \times 10° latitude) during MAM (March,
501 April, and May), JJA (June, July, and August), and SON (September, October, and November), as



502 highlighted in Figure 13, indicating relatively large model-satellite discrepancies in the region.
503 Moreover, this is also the region where the Nairobi ozonesonde site and the Kampala surface PM_{2.5}
504 site are located (Figure 1b). As discussed above, both MUSICAv0 and WRF-Chem significantly
505 overestimate O₃ (Figure 9) and largely underestimate PM_{2.5} (Figure 10) in the region. More in situ
506 observations or future field campaigns in the region can substantially help in the understanding
507 model-satellite and model-in situ observation discrepancies and improving model performance.

508 The 30°E – 45°E, 5°S – 5°N region in East Africa is potentially a favorable location for
509 future field campaign(s) not only because of the large model-satellite and model-in situ observation
510 discrepancies, but also due to that the population density is high and landcover are diverse in the
511 region (Figure 8). The relatively high population density in the region indicates that improved air
512 quality modeling in the region can benefit a large population. And a diverse landcover indicates
513 more processes/environments can be sampled. CO tracers in the model (Figure 14) show that CO
514 over the region is mainly driven by both anthropogenic and fire emissions. Anthropogenic
515 emissions play a more important role in this region compared to East Africa in general (Figures 4
516 and 14). In terms of source regions, emissions from East Africa and inflow from outside the
517 continent are the dominant source, with some contributions from Central Africa. Note that the
518 source analyses using model tracers may be subject to uncertainties in the emission inventories.
519 As discussed above (e.g., Section 3.4), there might be missing sources in the region. Therefore, a
520 field campaign in the region can help address this issue.

521 We would like to point out that in this analysis, the key area is selected using 3 satellite
522 products/chemical species and two models. The Taylor score is a comprehensive measure of model
523 performance that accounts for variance and correlation, however, other models and types of
524 comparisons may provide different answers.
525

526 5. Conclusions

527 Africa is one of the most rapidly changing regions in the world and air pollution is a
528 growing issue at multiple scales over the continent. MUSICAv0 is a new community modeling
529 infrastructure that enables the study of atmospheric composition and chemistry across all relevant
530 scales. We developed a MUSICAv0 grid with Africa refinement (~28 km × 28 km over Africa and
531 ~110 km × 110 km for the rest of the world) and conducted the simulation for the year 2017. We
532 evaluated the model with in situ observations including ATom-2 and ATom-3 airborne
533 measurements of CO, NO, and O₃, IAGOS airborne measurements of CO and O₃, O₃ profiles from
534 ozonesondes, surface CO observations from WDGCC, and surface PM_{2.5} observations from two
535 U.S. Embassy locations. We then compare MUSICAv0 with satellite products over Africa, namely
536 MOPITT CO column, MODIS AOD, OMI tropospheric NO₂ column, and OMI tropospheric
537 HCHO column. Results from a WRF-Chem simulation were also included in the evaluations and
538 comparisons as a reference. Lastly, as an application of the model, we identified potential African
539 regions for in situ observations and field campaign(s) based on model-satellite discrepancies
540 (quantified by Taylor score), with regard to model-in situ observation discrepancies, source
541 analyses, population, and land cover. The main conclusions are as follows.

542 (1) When comparing to ATom-2 and ATom-3, MUSICAv0 consistently underestimates
543 CO globally. Overall, the negative model bias increases with latitude from the Southern
544 Hemisphere to the Northern Hemisphere. MUSICAv0 also tends to overestimate O₃ in the
545 stratosphere/UTLS, and the positive model bias overall decreases with altitude.



- 546 (2) The MUSICAv0 biases in O₃ when compared to ATom, IAGOS, and ozonesondes are
547 likely driven by stratosphere-to-troposphere fluxes of O₃ and lightning NO emissions.
- 548 (3) Overall, the performance of MUSICAv0 and WRF-Chem are similar when compared
549 to the surface CO observations from six WDCGG sites in Africa.
- 550 (4) Both models have negative bias compared to the MOPITT CO column, especially over
551 Central Africa in September, which is likely driven by fires.
- 552 (5) Overall, MUSICAv0 agrees better with OMI tropospheric NO₂ column than WRF-
553 Chem.
- 554 (6) MUSICAv0 overall has a lower tropospheric HCHO column than OMI retrievals in all
555 regions and seasons. Biogenic and fire emissions are likely to be the main driver of this
556 disagreement.
- 557 (7) Over Africa, the MUSICAv0 simulation has smaller mean bias and RMSE compared
558 to MODIS AOD than the WRF-Chem simulation.
- 559 (8) The 30°E – 45°E, 5°S – 5°N region in East Africa is potentially a favorable location for
560 future field campaign(s) not only because of the large model-satellite and model-in situ
561 observation discrepancies, but also due to the population density, landcover, and pollution
562 source in this region.

563 Overall, the performance of MUSICAv0 is comparable to WRF-Chem. The
564 underestimation of CO is a common issue in atmospheric chemistry models such as MUSICAv0
565 and WRF-Chem. The overestimation of O₃ in MUSICAv0 is likely driven by too strong of
566 stratosphere-to-troposphere fluxes of O₃ and perhaps an over-estimate of lightning NO emissions,
567 however, future studies are needed to confirm and solve this issue. The significant underestimation
568 in surface PM_{2.5} at two sites in East Africa and the overall overestimation in AOD in Africa
569 compared to MODIS imply missing local sources and an overestimation of dust emissions, and
570 require further study. Field campaigns and more in situ observations in 30°E–45°E, 5°S–5°N
571 region in East Africa are necessary for the improvement of atmospheric chemistry model(s) as
572 shown by the MUSICAv0 and WRF-Chem simulations. In the future, we plan to conduct a model
573 simulation for multiple years and develop additional model grids with potentially higher resolution
574 in Africa sub-regions based on the current MUSICAv0 Africa grid.

575

576 **Code and data availability**

577 The MUSICAv0 model source code and the model documentation can be downloaded through
578 <https://wiki.ucar.edu/display/MUSICA/MUSICA+Home> (last access: 3 April 2023). CAMS-
579 GLOB-ANTH version 5.1 emissions can be found at <https://eccad3.sedoo.fr/data> (last access: 3
580 April 2023). QFED emissions can be found at
581 <https://portal.nccs.nasa.gov/datashare/ies/aerosol/emissions/QFED/> (last access: 3 April 2023).
582 MERRA-2 data can be found at <https://disc.gsfc.nasa.gov/datasets?project=MERRA-2> (last
583 access: 3 April 2023). ATom data are available at
584 <https://espoarchive.nasa.gov/archive/browse/atom> (last access: 3 April 2023). WDCGG data are
585 available at <https://gaw.kishou.go.jp/> (last access: 3 April 2023). IAGOS data are available at
586 <https://www.iagos.org/iagos-data/> (last access: 3 April 2023). NASA/GSFC SHADOZ data are
587 available at <https://tropo.gsfc.nasa.gov/shadoz/> (last access: 3 April 2023). The surface PM_{2.5} data



588 used in this study are available through data are available through
589 <https://www.airnow.gov/international/us-embassies-and-consulates/> (last access: 3 April 2023).
590 MOPITT CO and MODIS AOD data can be accessed through
591 <https://search.earthdata.nasa.gov/search> (last access: 3 April 2023). OMI NO₂ and OMI HCHO
592 data are available at <https://www.temis.nl/qa4ecv/no2.html> (last access: 3 April 2023) and
593 <https://www.temis.nl/qa4ecv/hcho.html> (last access: 3 April 2023), respectively.

594

595 **Acknowledgement**

596 This material is based upon work partially supported by the National Aeronautics and Space
597 Administration under Grant No. 80NSSC23K0181 issued through the NASA Applied Sciences
598 SERVIR program. We thank ATom, WDCGG, IAGOS, NASA/GSFC SHADOZ teams, and the
599 U.S. State Department and the U.S. EPA for in situ observations. We thank Anne Thompson and
600 Gonzague Romanens for detailed explanation of SHADOZ Ozonesonde data format. We thank
601 MOPITT, MODIS AOD, OMI NO₂ and OMI HCHO teams for the satellite products. The NCAR
602 MOPITT project is supported by the National Aeronautics and Space Administration (NASA)
603 Earth Observing System (EOS) program. We thank the QA4ECV project. We thank Sabine Darras
604 for CAMSv5.1 emissions. We would like to acknowledge high-performance computing support
605 from Cheyenne (doi:10.5065/D6RX99HX) provided by NCAR's Computational and Information
606 Systems Laboratory, sponsored by the National Science Foundation. This material is based upon
607 work supported by the National Center for Atmospheric Research, which is a major facility
608 sponsored by the National Science Foundation under Cooperative Agreement No. 1852977. We
609 thank James Hannigan, Ivan Ortega, Siyuan Wang, and all the attendees of ACOM CAM-
610 chem/MUSICA weekly meeting for helpful discussions.

611

612 **Competing interests**

613 The contact author has declared that neither they nor their co-authors have any competing
614 interests.

615

616 **Author contributions**

617 WT, LKE, HMW, and PL were involved in the initial design of this study. WT led the analysis.
618 RK and CH conducted the WRF-Chem simulation. ZZ interpreted PM_{2.5} results. BG, ST, SM
619 and other coauthors provide discussions. RRB helped with QFED emissions. CG and AS produced
620 CAMSv5.1 emissions. KM, BCD, JP, and CT conducted measurements during ATom. WT
621 prepared the paper with improvements from all coauthors.

622

623

624 **Reference**

625 Baudoin, M.A., Vogel, C., Nortje, K. and Naik, M., 2017. Living with drought in South Africa:
626 lessons learnt from the recent El Niño drought period. *International journal of disaster risk*
627 *reduction*, 23, pp.128-137.

628 Bauer, S. E., Im, U., Mezuman, K., & Gao, C. Y. (2019). Desert dust, industrialization, and
629 agricultural fires: Health impacts of outdoor air pollution in Africa. *Journal of Geophysical*
630 *Research: Atmospheres*, 124, 4104– 4120. <https://doi.org/10.1029/2018JD029336>.



- 631 Boone, A.A., Xue, Y., De Sales, F., Comer, R.E., Hagos, S., Mahanama, S., Schiro, K., Song, G.,
632 Wang, G., Li, S. and Mechoso, C.R., 2016. The regional impact of Land-Use Land-cover Change
633 (LULCC) over West Africa from an ensemble of global climate models under the auspices of the
634 WAMME2 project. *Climate Dynamics*, 47(11), pp.3547-3573.
- 635 Brown, F., Folberth, G. A., Sitch, S., Bauer, S., Bauters, M., Boeckx, P., Cheesman, A. W., Deushi,
636 M., Dos Santos Vieira, I., Galy-Lacaux, C., Haywood, J., Keeble, J., Mercado, L. M., O'Connor,
637 F. M., Oshima, N., Tsigaridis, K., and Verbeeck, H., 2022. The ozone–climate penalty over South
638 America and Africa by 2100, *Atmos. Chem. Phys.*, 22, 12331–12352, <https://doi.org/10.5194/acp-22-12331-2022>.
639
640
- 641 Boersma, K. F., Eskes, H., Richter, A., De Smedt, I., Lorente, A., Beirle, S., Van Geffen, J., Peters,
642 E., Van Roozendaal, M. and Wagner, T., (2017a). QA4ECV NO₂ tropospheric and stratospheric
643 vertical column data from OMI (Version 1.1). Royal Netherlands Meteorological Institute
644 (KNMI). <http://doi.org/10.21944/qa4ecv-no2-omi-v1.1>.
645
- 646 Boersma, K.F., van Geffen, J., Eskes, H., van der A, R., De Smedt, I. and Van Roozendaal, M.,
647 2017b. Product specification document for the QA4ECV NO₂ ECV precursor product.
648
- 649 Bourgeois, I., Peischl, J., Thompson, C. R., Aikin, K. C., Campos, T., Clark, H., Commane, R.,
650 Daube, B., Diskin, G. W., Elkins, J. W., Gao, R.-S., Gaudel, A., Hints, E. J., Johnson, B. J., Kivi,
651 R., McKain, K., Moore, F. L., Parrish, D. D., Querel, R., Ray, E., Sánchez, R., Sweeney, C.,
652 Tarasick, D. W., Thompson, A. M., Thouret, V., Witte, J. C., Wofsy, S. C., and Ryerson, T. B.:
653 Global-scale distribution of ozone in the remote troposphere from the ATom and HIPPO airborne
654 field missions, *Atmos. Chem. Phys.*, 20, 10611–10635, <https://doi.org/10.5194/acp-20-10611-2020>, 2020.
655
656
- 657 Bourgeois, I., Peischl, J., Neuman, J.A., Brown, S.S., Thompson, C.R., Aikin, K.C., Allen, H.M.,
658 Angot, H., Apel, E.C., Baublitz, C.B. and Brewer, J.F., 2021. Large contribution of biomass
659 burning emissions to ozone throughout the global remote troposphere. *Proceedings of the National
660 Academy of Sciences*, 118(52), p.e2109628118.
661
- 662 Center for International Earth Science Information Network (CIESIN), Columbia University.
663 2018. Documentation for the Gridded Population of the World, Version 4 (GPWv4), Revision 11
664 Data Sets. Palisades NY: NASA Socioeconomic Data and Applications Center (SEDAC).
665 <https://doi.org/10.7927/H45Q4T5F> Accessed 2022-11-17.
- 666 Chin, M., Ginoux, P., Kinne, S., Torres, O., Holben, B.N., Duncan, B.N., Martin, R.V., Logan,
667 J.A., Higurashi, A., Nakajima, T., 2002. Tropospheric aerosol optical thickness from the GOCART
668 model and comparisons with satellite and sun photometer measurements. *J. Atmos. Sci.* 59, 461–
669 483. [https://doi.org/10.1175/1520-0469\(2002\)059<0461:TAOTFT>2.0.CO;2](https://doi.org/10.1175/1520-0469(2002)059<0461:TAOTFT>2.0.CO;2).
- 670 Clarke, K., Ash, K., Coker, E.S., Sabo-Attwood, T. and Bainomugisha, E., 2022. A Social
671 Vulnerability Index for Air Pollution and Its Spatially Varying Relationship to PM_{2.5} in Uganda.
672 *Atmosphere*, 13(8), p.1169.



- 673 Compernolle, S., Verhoelst, T., Pinardi, G., Granville, J., Hubert, D., Keppens, A., Niemeijer, S.,
674 Rino, B., Bais, A., Beirle, S., Boersma, F., Burrows, J. P., De Smedt, I., Eskes, H., Goutail, F.,
675 Hendrick, F., Lorente, A., Pazmino, A., Piters, A., Peters, E., Pommereau, J.-P., Remmers, J.,
676 Richter, A., van Geffen, J., Van Roozendael, M., Wagner, T., and Lambert, J.-C.: Validation of
677 Aura-OMI QA4ECV NO₂ climate data records with ground-based DOAS networks: the role of
678 measurement and comparison uncertainties, *Atmos. Chem. Phys.*, 20, 8017–8045,
679 <https://doi.org/10.5194/acp-20-8017-2020>, 2020.
- 680 Darmenov, A., & da Silva, A. (2013). The quick fire emissions dataset (QFED)—documentation of
681 versions 2.1, 2.2 and 2.4. NASA Technical Report Series on Global Modeling and Data
682 Assimilation, NASA TM-2013-104606, 32, 183.
- 683 De Longueville, F., Hountondji, Y.C., Henry, S. and Ozer, P., 2010. What do we know about
684 effects of desert dust on air quality and human health in West Africa compared to other regions?.
685 *Science of the total environment*, 409(1), pp.1-8.
- 686 De Smedt, I., Yu, H., Richter, A., Beirle, S., Eskes, H., Boersma, K.F., Van Roozendael, M., Van
687 Geffen, J., Lorente, A. and Peters, E., (2017a), QA4ECV HCHO tropospheric column data from
688 OMI (Version 1.1). Royal Belgian Institute for Space Aeronomy.
689 <http://doi.org/10.18758/71021031>.
- 690 De Smedt, I., Van Geffen, J., Richter, A., Beirle S., Yu, H., Vlietinck J., Van Roozendael, M. van
691 der A R., Lorente A., Scanlon T., Compernolle S., Wagner T., Boersma, K. F., Eskes, H., 2017b,
692 Product User Guide for HCHO.
- 693 Deeter, M.N., 2009. MOPITT (Measurements of Pollution in the Troposphere) Validated Version
694 4 Product User's Guide. National Centre for Atmospheric Research, Boulder, CO, 80307.
- 695 Deeter, M. N., Worden, H. M., Gille, J. C., Edwards, D. P., Mao, D., and Drummond, J. R.:
696 MOPITT multispectral CO retrievals: Origins and effects of geophysical radiance errors, *J.*
697 *Geophys. Res.*, 116, D15303, <https://doi.org/10.1029/2011JD015703>, 2011.
- 698 Deeter, M., Francis, G., Gille, J., Mao, D., Martínez-Alonso, S., Worden, H., Ziskin, D.,
699 Drummond, J., Commane, R., Diskin, G., and McKain, K.: The MOPITT Version 9 CO product:
700 sampling enhancements and validation, *Atmos. Meas. Tech.*, 15, 2325–2344,
701 <https://doi.org/10.5194/amt-15-2325-2022>, 2022.
- 702 Emmons, L.K., Walters, S., Hess, P.G., Lamarque, J.-F., Pfister, G.G., Fillmore, D., Granier, C.,
703 Guenther, A., Kinnison, D., Laepple, T., Orlando, J., Tie, X., Tyndall, G., Wiedinmyer, C.,
704 Baughcum, S.L., Kloster, S., 2010. Description and evaluation of the model for ozone and related
705 chemical tracers, version 4 (MOZART-4). *Geosci. Model Dev.* 3, 43–67.
706 <https://doi.org/10.5194/gmd-3-43-2010>.
- 707 Emmons, L.K., Schwantes, R. H., Orlando, J. J., Tyndall, G., Kinnison, D., Lamarque, J.-F., et al.:
708 The Chemistry Mechanism in the Community Earth System Model version 2 (CESM2), *Journal*
709 *of Advances in Modeling Earth Systems*, 12, <https://doi.org/10.1029/2019MS001882>, 2020.



- 710 Fisher, J. A., Murray, L. T., Jones, D. B. A., & Deutscher, N. M. (2017). Improved method for
711 linear carbon monoxide simulation and source attribution in atmospheric chemistry models
712 illustrated using GEOS-Chem v9. *Geoscientific Model Development*, 10, 4129–4144.
713 <https://doi.org/10.5194/gmd-10-4129-2017>.
- 714 Fisher, S., Bellinger, D.C., Cropper, M.L., Kumar, P., Binagwaho, A., Koudenoukpo, J.B., Park,
715 Y., Taghian, G. and Landrigan, P.J., 2021. Air pollution and development in Africa: impacts on
716 health, the economy, and human capital. *The Lancet Planetary Health*, 5(10), pp.e681-e688.
- 717 Friedl, M., D. Sulla-Menashe. MODIS/Terra+Aqua Land Cover Type Yearly L3 Global 0.05Deg
718 CMG V061. 2022, distributed by NASA EOSDIS Land Processes DAAC,
719 <https://doi.org/10.5067/MODIS/MCD12C1.061>. Accessed 2022-11-17.
- 720 Gaubert, B., Arellano, A. F., Barré, J., Worden, H. M., Emmons, L. K., Tilmes, S., Buchholz, R.
721 R., Vitt, F., Raeder, K., Collins, N., Anderson, J. L., Wiedinmyer, C., Martínez-Alonso, S.,
722 Edwards, D. P., Andreae, M. O., Hannigan, J. W., Petri, C., Strong, K., and Jones, N.: Toward a
723 chemical reanalysis in a coupled chemistry-climate model: An evaluation of MOPITT CO
724 assimilation and its impact on tropospheric composition, *J. Geophys. Res.-Atmos.*, 121, 7310–
725 7343, <https://doi.org/10.1002/2016JD024863>, 2016.
- 726 Gaubert, B., Emmons, L. K., Raeder, K., Tilmes, S., Miyazaki, K., Arellano Jr., A. F., Elguindi,
727 N., Granier, C., Tang, W., Barré, J., Worden, H. M., Buchholz, R. R., Edwards, D. P., Franke, P.,
728 Anderson, J. L., Saunio, M., Schroeder, J., Woo, J.-H., Simpson, I. J., Blake, D. R., Meinardi, S.,
729 Wennberg, P. O., Crounse, J., Teng, A., Kim, M., Dickerson, R. R., He, H., Ren, X., Pusede, S. E.,
730 and Diskin, G. S.: Correcting model biases of CO in East Asia: impact on oxidant distributions
731 during KORUS-AQ, *Atmos. Chem. Phys.*, 20, 14617–14647, [https://doi.org/10.5194/acp-20-](https://doi.org/10.5194/acp-20-14617-2020)
732 14617-2020, 2020.
- 733 Gelaro, R., McCarty, W., Suárez, M. J., Todling, R., Molod, A., Takacs, L., et al. (2017). The
734 modern-era retrospective analysis for research and applications, version 2 (MERRA-2). *Journal of*
735 *Climate*, 30(14), 5419-5454.
- 736 Güneralp, B., Lwasa, S., Masundire, H., Parnell, S. and Seto, K.C., 2017. Urbanization in Africa:
737 challenges and opportunities for conservation. *Environmental research letters*, 13(1), p.015002.
- 738 Heft-Neal, S., Burney, J., Bendavid, E. and Burke, M., 2018. Robust relationship between air
739 quality and infant mortality in Africa. *Nature*, 559(7713), pp.254-258.
- 740 Hsu, N.C., Jeong, M.J., Bettenhausen, C., Sayer, A.M., Hansell, R., Seftor, C.S., Huang, J. and
741 Tsay, S.C., 2013. Enhanced Deep Blue aerosol retrieval algorithm: The second generation. *Journal*
742 *of Geophysical Research: Atmospheres*, 118(16), pp.9296-9315.
- 743 Jo, D., et al., Effects of Grid Resolution and Emission Inventory on Urban Air Quality Simulation
744 With the Multi-Scale Infrastructure for Chemistry and Aerosols (MUSICA) Version 0, JAMES,
745 in review, 2022.
- 746 Kuik, F., Lauer, A., Beukes, J. P., Van Zyl, P. G., Josipovic, M., Vakkari, V., Laakso, L., and Feig,
747 G. T.: The anthropogenic contribution to atmospheric black carbon concentrations in southern



- 748 Africa: a WRF-Chem modeling study, *Atmos. Chem. Phys.*, 15, 8809–8830,
749 <https://doi.org/10.5194/acp-15-8809-2015>, 2015.
- 750 Kumar, R., He, C., Bhardwaj, P., Lacey, F., Buchholz, R.R., Brasseur, G.P., Joubert, W.,
751 Labuschagne, C., Kozlova, E. and Mkololo, T., 2022. Assessment of regional carbon monoxide
752 simulations over Africa and insights into source attribution and regional transport. *Atmospheric*
753 *Environment*, 277, p.119075.
- 754 Lacey, F. G., Marais, E. A., Henze, D. K., Lee, C. J., van Donkelaar, A., Martin, R. V., et al. (2017).
755 Improving present day and future estimates of anthropogenic sectoral emissions and the resulting
756 air quality impacts in Africa. *Faraday Discussions*, 200, 397–412.
757 <https://doi.org/10.1039/C7FD00011A>.
- 758 Lauritzen, P. H., Nair, R. D., Herrington, A. R., Callaghan, P., Goldhaber, S., Dennis, J. M.,
759 Bacmeister, J. T., Eaton, B. E., Zarzycki, C. M., Taylor, M. A., Ullrich, P. A., Dubos, T., Gettelman,
760 A., Neale, R. B., Dobbins, B., Reed, K. A., Hannay, C., Medeiros, B., Benedict, J. J. and Tribbia,
761 J. J.: NCAR Release of CAM-SE in CESM2.0: A Reformulation of the Spectral Element
762 Dynamical Core in Dry-Mass Vertical Coordinates With Comprehensive Treatment of
763 Condensates and Energy, *Journal of Advances in Modeling Earth Systems*, 10(7), 1537–1570,
764 2018.
- 765 Levy, R. C., Mattoo, S., Munchak, L. A., Remer, L. A., Sayer, A. M., Patadia, F., and Hsu, N. C.:
766 The Collection 6 MODIS aerosol products over land and ocean, *Atmos. Meas. Tech.*, 6, 2989–
767 3034, <https://doi.org/10.5194/amt-6-2989-2013>, 2013.
- 768 Levy, R., Hsu, C., et al., 2017. MODIS Atmosphere L2 Aerosol Product. NASA MODIS Adaptive
769 Processing System, Goddard Space Flight Center, USA:
770 http://dx.doi.org/10.5067/MODIS/MOD04_L2.061.
- 771 Liousse, C., Assamoi, E., Criqui, P., Granier, C., and Rosset, R.: Explosive growth in African
772 combustion emissions from 2005 to 2030, *Environ. Res. Lett.*, 9, 35003,
773 <https://doi.org/10.1088/1748-9326/9/3/035003>, 2014.
- 774 Liu, J. C., Mickley, L. J., Sulprizio, M. P., Dominici, F., Yue, X., Ebisu, K., ... & Bell, M. L. (2016).
775 Particulate air pollution from wildfires in the Western US under climate change. *Climatic change*,
776 138(3), 655-666.
- 777 Malings, C., Westervelt, D. M., Hauryliuk, A., Presto, A. A., Grieshop, A., Bittner, A., Beekmann,
778 M., and R. Subramanian: Application of low-cost fine particulate mass monitors to convert satellite
779 aerosol optical depth to surface concentrations in North America and Africa, *Atmos. Meas. Tech.*,
780 13, 3873–3892, <https://doi.org/10.5194/amt-13-3873-2020>, 2020.
- 781 Marais, E. A., Jacob, D. J., Kurosu, T. P., Chance, K., Murphy, J. G., Reeves, C., Mills, G., Casadio,
782 S., Millet, D. B., Barkley, M. P., Paulot, F., and Mao, J.: Isoprene emissions in Africa inferred
783 from OMI observations of formaldehyde columns, *Atmos. Chem. Phys.*, 12, 6219–6235,
784 <https://doi.org/10.5194/acp-12-6219-2012>, 2012.



- 785 Marais, E.A., Silvern, R.F., Vodonos, A., Dupin, E., Bockarie, A.S., Mickley, L.J. and Schwartz,
786 J., 2019. Air quality and health impact of future fossil fuel use for electricity generation and
787 transport in Africa. *Environmental science & technology*, 53(22), pp.13524-13534.
- 788 Mazzeo, A., Burrow, M., Quinn, A., Marais, E. A., Singh, A., Ng'ang'a, D., Gatari, M. J., and Pope,
789 F. D.: Evaluation of the WRF and CHIMERE models for the simulation of PM_{2.5} in large East
790 African urban conurbations, *Atmos. Chem. Phys.*, 22, 10677–10701, [https://doi.org/10.5194/acp-](https://doi.org/10.5194/acp-22-10677-2022)
791 22-10677-2022, 2022.
- 792 Menut, L., Flamant, C., Turquety, S., Deroubaix, A., Chazette, P., and Meynadier, R.: Impact of
793 biomass burning on pollutant surface concentrations in megacities of the Gulf of Guinea, *Atmos.*
794 *Chem. Phys.*, 18, 2687–2707, <https://doi.org/10.5194/acp-18-2687-2018>, 2018.
- 795 Nicholson, S.E., 2019. A review of climate dynamics and climate variability in Eastern Africa.
796 The limnology, climatology and paleoclimatology of the East African lakes, pp.25-56.
- 797 Paton-Walsh, C., Emmerson, K.M., Garland, R.M., Keywood, M., Hoelzemann, J.J., Huneus, N.,
798 Buchholz, R.R., Humphries, R.S., Altieri, K., Schmale, J. and Wilson, S.R., 2022. Key challenges
799 for tropospheric chemistry in the Southern Hemisphere. *Elem Sci Anth*, 10(1), p.00050.
- 800 Petkova, E.P., Jack, D.W., Volavka-Close, N.H. and Kinney, P.L., 2013. Particulate matter
801 pollution in African cities. *Air Quality, Atmosphere & Health*, 6(3), pp.603-614.
- 802 Petzold, A., Thouret, V., Gerbig, C., Zahn, A., Brenninkmeijer, C.A., Gallagher, M., Hermann,
803 M., Pontaud, M., Ziereis, H., Boulanger, D. and Marshall, J., 2015. Global-scale atmosphere
804 monitoring by in-service aircraft—current achievements and future prospects of the European
805 Research Infrastructure IAGOS. *Tellus B: Chemical and Physical Meteorology*, 67(1), p.28452.
- 806 Pfister, G. G., Eastham, S. D., Arellano, A. F., Aumont, B., Barsanti, K. C., Barth, M. C., ... &
807 Brasseur, G. P. (2020). The Multi-Scale Infrastructure for Chemistry and Aerosols (MUSICA).
808 *Bulletin of the American Meteorological Society*, 101(10), E1743-E1760.
- 809 Schwantes, R.H., Lacey, F.G., Tilmes, S., Emmons, L.K., Lauritzen, P.H., Walters, S., Callaghan,
810 P., Zarzycki, C.M., Barth, M.C., Jo, D.S. and Bacmeister, J.T., 2022. Evaluating the impact of
811 chemical complexity and horizontal resolution on tropospheric ozone over the conterminous US
812 with a global variable resolution chemistry model. *Journal of Advances in Modeling Earth Systems*,
813 14(6), p.e2021MS002889.
- 814 Shindell, D. T., Faluvegi, G., Stevenson, D. S., Krol, M. C., Emmons, L. K., Lamarque, J. F., et
815 al. (2006). Multimodel simulations of carbon monoxide: Comparison with observations and
816 projected near-future changes. *Journal of Geophysical Research*, 111.
- 817 Soulie, A., C. Granier, S. Darras, T. Doumbia, M. Guevara, J.-P. Jalkanen, S. Keita, C. Liousse,
818 Global anthropogenic emissions (CAM5-GLOB-ANT) for the Copernicus Atmosphere
819 Monitoring Service Air Quality Forecasts and Reanalysis, to be submitted to *Earth Sys. Sci. data*,
820 2023.



- 821 Stauffer, R.M., Thompson, A.M., Kollonige, D.E., Witte, J.C., Tarasick, D.W., Davies, J., Vömel,
822 H., Morris, G.A., Van Malderen, R., Johnson, B.J. and Querel, R.R., 2020. A post-2013 dropoff
823 in total ozone at a third of global ozonesonde stations: Electrochemical concentration cell
824 instrument artifacts?. *Geophysical Research Letters*, 47(11), p.e2019GL086791.
- 825 Stein, O., Schultz, M. G., Bouarar, I., Clark, H., Huijnen, V., Gaudel, A., et al. (2014). On the
826 wintertime low bias of Northern Hemisphere carbon monoxide found in global model simulations.
827 *Atmospheric Chemistry and Physics*, 14, 9295–9316.
- 828 Tang, W., Arellano, A. F., DiGangi, J. P., Choi, Y., Diskin, G. S., Agustí-Panareda, A., Parrington,
829 M., Massart, S., Gaubert, B., Lee, Y., Kim, D., Jung, J., Hong, J., Hong, J.-W., Kanaya, Y., Lee,
830 M., Stauffer, R. M., Thompson, A. M., Flynn, J. H., and Woo, J.-H.: Evaluating high-resolution
831 forecasts of atmospheric CO and CO₂ from a global prediction system during KORUS-AQ field
832 campaign, *Atmos. Chem. Phys.*, 18, 11007–11030, <https://doi.org/10.5194/acp-18-11007-2018>,
833 2018.
- 834 Tang, W., Emmons, L. K., Arellano Jr., A. F., Gaubert, B., Knote, C., Tilmes, S., Buchholz, R. R.,
835 Pfister, G. G., Diskin, G. S., Blake, D. R., Blake, N. J., Meinardi, S., DiGangi, J. P., Choi, Y., Woo,
836 J.-H., He, C., Schroeder, J. R., Suh, I., Lee, H.-J., Jo, H.-Y., Kanaya, Y., Jung, J., Lee, Y., and Kim,
837 D.: Source contributions to carbon monoxide concentrations during KORUS-AQ based on CAM-
838 chem model applications, *J. Geophys. Res.-Atmos.*, 124, 1–27,
839 <https://doi.org/10.1029/2018jd029151>, 2019.
- 840 Tang, W., Emmons, L.K., Buchholz, R.R., Wiedinmyer, C., Schwantes, R.H., He, C., Kumar, R.,
841 Pfister, G.G., Worden, H.M., Hornbrook, R.S. and Apel, E.C., 2022. Effects of Fire Diurnal
842 Variation and Plume Rise on US Air Quality During FIREX-AQ and WE-CAN Based on the
843 Multi-Scale Infrastructure for Chemistry and Aerosols (MUSICAv0). *Journal of Geophysical
844 Research: Atmospheres*, 127(16), p.e2022JD036650.
- 845 Taylor, K. E. (2001). Summarizing multiple aspects of model performance in a single diagram.
846 *Journal of Geophysical Research*, 106(1755), 7183–7192. <https://doi.org/10.1029/2000JD900719>.
- 847 Thompson, A. M., Balashov, N. V., Witte, J. C., Coetzee, J. G. R., Thouret, V., and Posny, F.:
848 Tropospheric ozone increases over the southern Africa region: bellwether for rapid growth in
849 Southern Hemisphere pollution?, *Atmos. Chem. Phys.*, 14, 9855–9869,
850 <https://doi.org/10.5194/acp-14-9855-2014>, 2014.
- 851 Thompson, A. M., J. C. Witte, C., Sterling, A., Jordan, B. J., Johnson, S. J. Oltmans, ... Thiongo,
852 K. (2017). First reprocessing of Southern Hemisphere Additional Ozonesondes (SHADOZ) ozone
853 profiles (1998-2016): 2. Comparisons with satellites and ground-based instruments. *Journal of
854 Geophysical Research: Atmospheres*, 122, 13,000-13,025. <https://doi.org/10.1002/2017JD027406>.
- 855 Thompson, C. R., Wofsy, S. C., Prather, M. J., Newman, P. A., Hanisco, T. F., Ryerson, T. B.,
856 Fahey, D. W., Apel, E. C., Brock, C. A., Brune, W. H., Froyd, K., Katich, J. M., Nicely, J. M.,
857 Peischl, J., Ray, E., Veres, P. R., Wang, S., Allen, H. M., Asher, E., Bian, H., Blake, D., Bourgeois,
858 I., Budney, J., Bui, T. P., Butler, A., Campuzano-Jost, P., Chang, C., Chin, M., Commane, R.,
859 Correa, G., Crouse, J. D., Daube, B., Dibb, J. E., DiGangi, J. P., Diskin, G. S., Dollner, M., Elkins,
860 J. W., Fiore, A. M., Flynn, C. M., Guo, H., Hall, S. R., Hannun, R. A., Hills, A., Hints, E. J.,



- 861 Hodzic, A., Hornbrook, R. S., Huey, L. G., Jimenez, J. L., Keeling, R. F., Kim, M. J., Kupc, A.,
862 Lacey, F., Lait, L. R., Lamarque, J., Liu, J., McKain, K., Meinardi, S., Miller, D. O., Montzka, S.
863 A., Moore, F. L., Morgan, E. J., Murphy, D. M., Murray, L. T., Nault, B. A., Neuman, J. A.,
864 Nguyen, L., Gonzalez, Y., Rollins, A., Rosenlof, K., Sargent, M., Schill, G., Schwarz, J. P., Clair,
865 J. M. S., Steenrod, S. D., Stephens, B. B., Strahan, S. E., Strode, S. A., Sweeney, C., Thames, A.
866 B., Ullmann, K., Wagner, N., Weber, R., Weinzierl, B., Wennberg, P. O., Williamson, C. J., Wolfe,
867 G. M., and Zeng, L.: The NASA Atmospheric Tomography (ATom) Mission: Imaging the
868 Chemistry of the Global Atmosphere, *B. Am. Meteorol. Soc.*, 103, E761–E790, 2022.
- 869 Tilmes, S., Lamarque, J. F., Emmons, L. K., Kinnison, D. E., Ma, P. L., Liu, X., et al. (2015).
870 Description and evaluation of tropospheric chemistry and aerosols in the Community Earth System
871 Model (CESM1. 2). *Geoscientific Model Development*, 8, 1395–1426.
- 872 Tilmes, S., Hodzic, A., Emmons, L. K., Mills, M. J., Gettelman, A., Kinnison, D. E., et al.: Climate
873 forcing and trends of organic aerosols in the Community Earth System Model (CESM2). *Journal*
874 *of Advances in Modeling Earth Systems*, 11, <https://doi.org/10.1029/2019MS001827>, 2019.
- 875 U.S. EPA: Quality Assurance Guidance Document 2.12: Monitoring PM_{2.5} in Ambient Air Using
876 Designated Reference or Class I Equivalent Methods, United States Environmental Protection
877 Agency, available at: <https://www3.epa.gov/ttnamti1/files/ambient/pm25/qa/m212.pdf> (last
878 access: 20 November 2022), 2016.
- 879 van der Werf, G. R., Randerson, J. T., Giglio, L., van Leeuwen, T. T., Chen, Y., Rogers, B. M.,
880 Mu, M., van Marle, M. J. E., Morton, D. C., Collatz, G. J., Yokelson, R. J., and Kasibhatla, P. S.,
881 2017. Global fire emissions estimates during 1997–2016, *Earth Syst. Sci. Data*, 9, 697–720,
882 <https://doi.org/10.5194/essd-9-697-2017>.
- 883 Vohra, K., Marais, E.A., Bloss, W.J., Schwartz, J., Mickley, L.J., Van Damme, M., Clarisse, L.
884 and Coheur, P.F., 2022. Rapid rise in premature mortality due to anthropogenic air pollution in
885 fast-growing tropical cities from 2005 to 2018. *Science Advances*, 8(14), p.eabm4435.
- 886 Washington, R., Harrison, M., Conway, D., Black, E., Challinor, A., Grimes, D., Jones, R., Morse,
887 A., Kay, G. and Todd, M., 2006. African climate change: taking the shorter route. *Bulletin of the*
888 *American Meteorological Society*, 87(10), pp.1355-1366.
- 889 Watson, J. G., Chow, J. C., Moosmüller, H., Green, M., Frank, N., and Pitchford, M.: Guidance
890 for using continuous monitors in PM_{2.5} monitoring networks, U.S. EPA Office of Air Quality
891 Planning and Standards, Triangle Park, NC., 1998.
- 892 Wiedinmyer, C., Akagi, S.K., Yokelson, R.J., Emmons, L.K., Al-Saadi, J.A., Orlando, J.J., Soja,
893 A.J., 2011. The Fire INventory from NCAR (FINN): a high resolution global model to estimate
894 the emissions from open burning. *Geosci. Model Dev.* 4, 625–641. [https://doi.org/10.5194/gmd-](https://doi.org/10.5194/gmd-4-625-2011)
895 [4-625-2011](https://doi.org/10.5194/gmd-4-625-2011).
- 896 Wiedinmyer, C., Yokelson, R. J., and Gullett, B. K.: Global emissions of trace gases, particulate
897 matter, and hazardous air pollutants from open burning of domestic waste, *Environ. Sci. Technol.*,
898 48, 9523–9530, <https://doi.org/10.1021/es502250z>, 2014.



899 Witte, J.C., A. M. Thompson, H. G. J. Smit, M. Fujiwara, F. Posny, Gert J. R. Coetzee, ... F. R. da
900 Silva (2017), First reprocessing of Southern Hemisphere ADditional OZonesondes (SHADOZ)
901 profile records (1998-2015): 1. Methodology and evaluation, *J. Geophys. Res. Atmos.*, 122, 6611-
902 6636. <https://doi.org/10.1002/2016JD026403>.

903 Witte, J. C., Thompson, A. M., Smit, H. G. J., Vömel, H., Posny, F., & Stübi, R. (2018). First
904 reprocessing of Southern Hemisphere ADditional OZonesondes profile records: 3. Uncertainty in
905 ozone profile and total column. *Journal of Geophysical Research: Atmospheres*, 123, 3243-3268.
906 <https://doi.org/10.1002/2017JD027791>.

907 Worden, H. M., Deeter, M. N., Edwards, D. P., Gille, J. C., Drummond, J. R., and Nédélec, P.:
908 Observations of near-surface carbon monoxide from space using MOPITT multispectral retrievals,
909 *J. Geophys. Res.*, 115, D18314, <https://doi.org/10.1029/2010JD014242>, 2010.

910 Ziervogel, G., New, M., Archer van Garderen, E., Midgley, G., Taylor, A., Hamann, R., Stuart-
911 Hill, S., Myers, J. and Warburton, M., 2014. Climate change impacts and adaptation in South
912 Africa. *Wiley Interdisciplinary Reviews: Climate Change*, 5(5), pp.605-620.

913

914

915

916

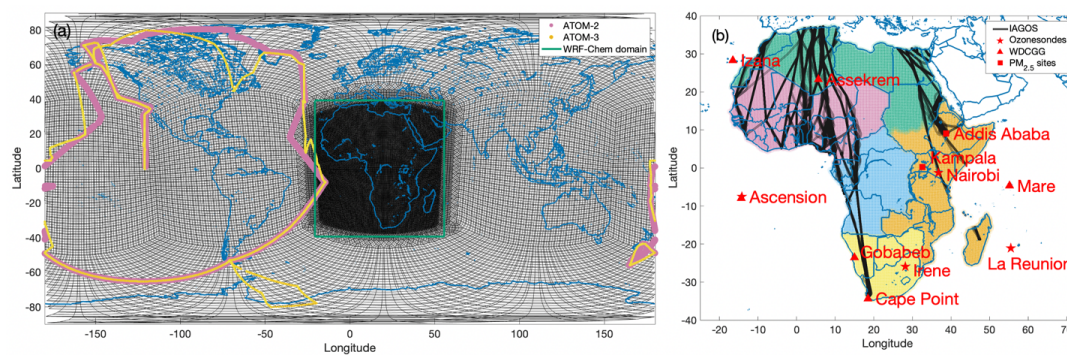
917

918

919

920

921



922

923

924

925

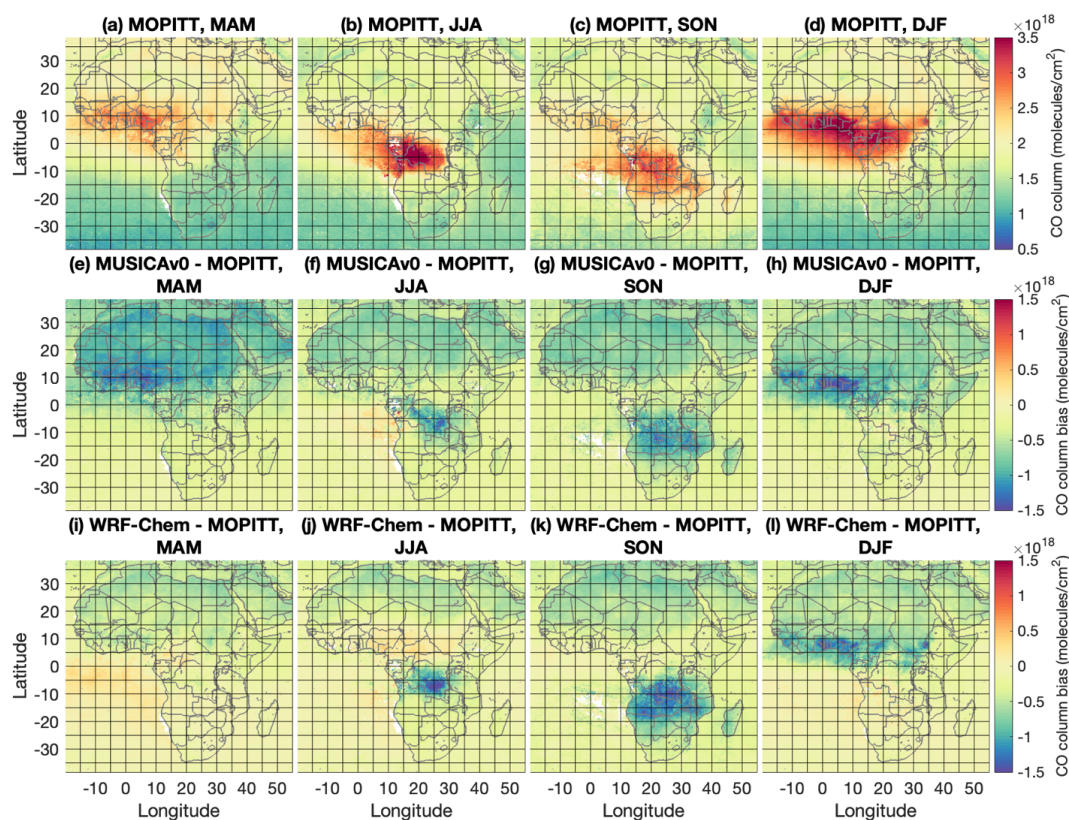
926

927

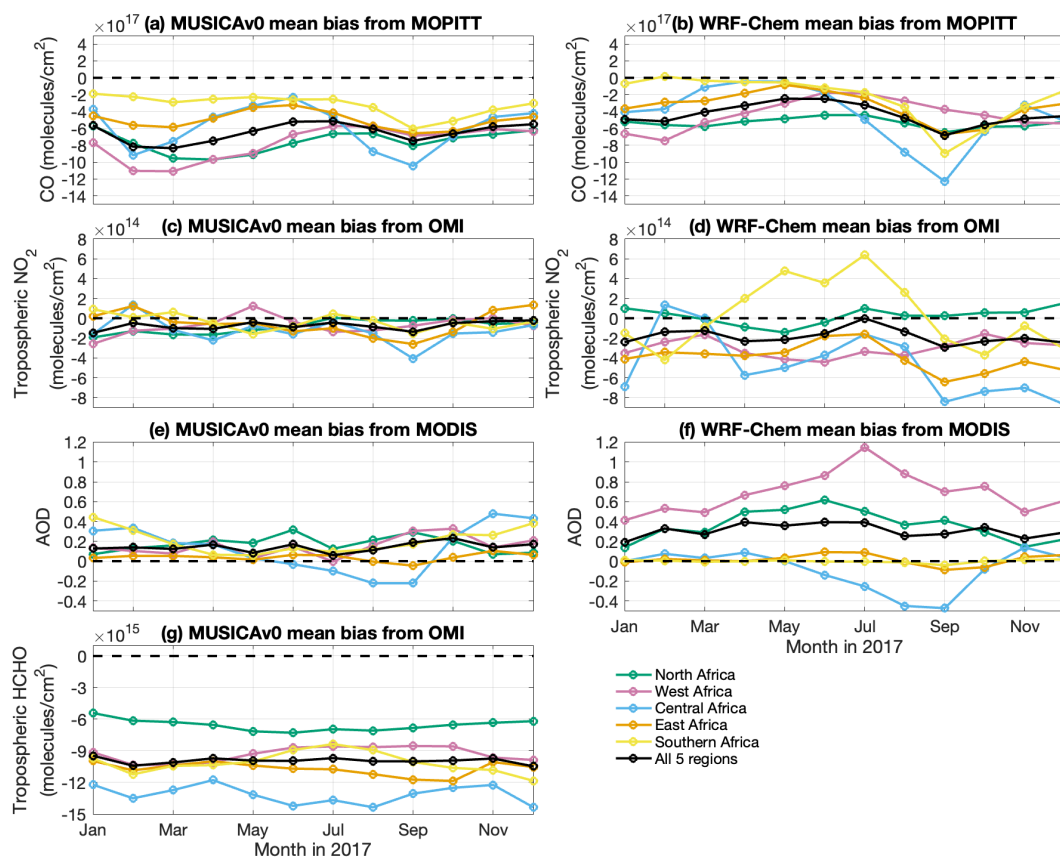
Figure 1. Model grid, in situ observations used in this study, and sub-regions in Africa. (a) MUSICAv0 model grid developed for Africa in this study (black), domain boundary of the WRF-Chem simulation compared in this study (shown by green box), observations from the Atmospheric Tomography Mission (ATom) field campaign 2 (ATom-2; 2017 Jan to 2017 Feb; pink) and ATom-3 (2017 Sep to 2017 Oct; yellow). (b) Sub-regions in Africa are shown, namely



928 North Africa (green), West Africa (pink), East Africa (orange), Central Africa (blue), and Southern
929 Africa (yellow). Location of in situ observations are labeled on the map. Flight tracks of the In-
930 service Aircraft for a Global Observing System (IAGOS) are shown with black lines. Four
931 ozonesonde sites are shown by pentagrams (Ascension, Irene, Nairobi, and La Reunion); six sites
932 from the World Data Centre for Greenhouse Gases are shown by triangles (Assekrem, Cape Point,
933 Izana, Gobabeb, Mare, and Ascension); two surface sites for PM_{2.5} are shown by squares (Addis
934 Ababa and Kampala).
935
936
937
938

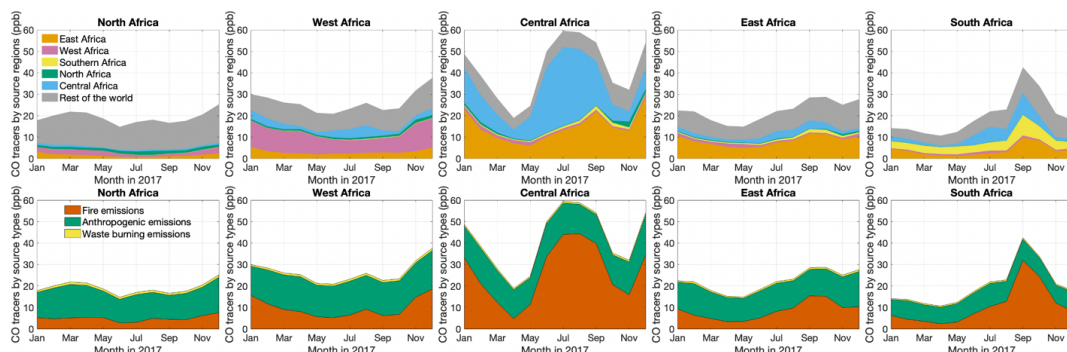


939
940 **Figure 2.** Comparisons of MUSICAv0 and WRF-Chem simulations to MOPITT CO column
941 (molecules/cm²) for each season of 2017. (a-d) Averaged MOPITT CO column: MAM (March,
942 April, and May), JJA (June, July, and August), SON (September, October, and November), and
943 DJF (December, January, and February). (e-h) MUSICAv0 model biases against MOPITT CO
944 column for MAM, JJA, SON, and DJF. (i-l) is the same as (e-h) but for WRF-Chem. All data are
945 gridded to 0.25 degree × 0.25 degree for plotting.
946
947



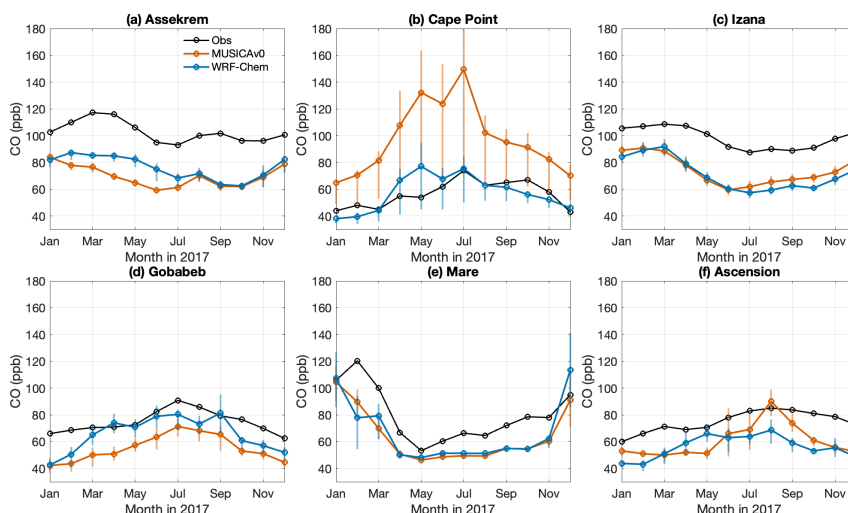
948
 949
 950
 951
 952
 953
 954
 955
 956
 957

Figure 3. Mean bias of MUSICA v0 and WRF-Chem simulations from satellite data. Monthly timeseries of mean bias of (a) MUSICA v0 and (b) WRF-Chem against MOPITT CO column (molecules/cm²) in 2017 over Africa (black), North Africa (green), West Africa (pink), East Africa (orange), Central Africa (blue), and Southern Africa (yellow). (c-d) are same as (a-b) but for mean bias against OMI tropospheric NO₂ column (molecules/cm²). (e-f) are same as (a-b) but for mean bias against with MODIS (Terra) Aerosol Optical Depth (AOD). (g) is the same as (a) but for mean bias against OMI tropospheric HCHO column (molecules/cm²).



958
 959
 960
 961
 962
 963
 964
 965

Figure 4. Monthly time series of column-averaged CO tracers in North Africa, West Africa, East Africa, Central Africa, and Southern Africa. Top panels show CO tracers of emissions from North Africa (green), West Africa (pink), East Africa (orange), Central Africa (blue), Southern Africa (yellow), and the rest of the world (grey). Bottom panels show CO tracers of fire emissions (red), anthropogenic emissions (green), and waste burning emissions (yellow).

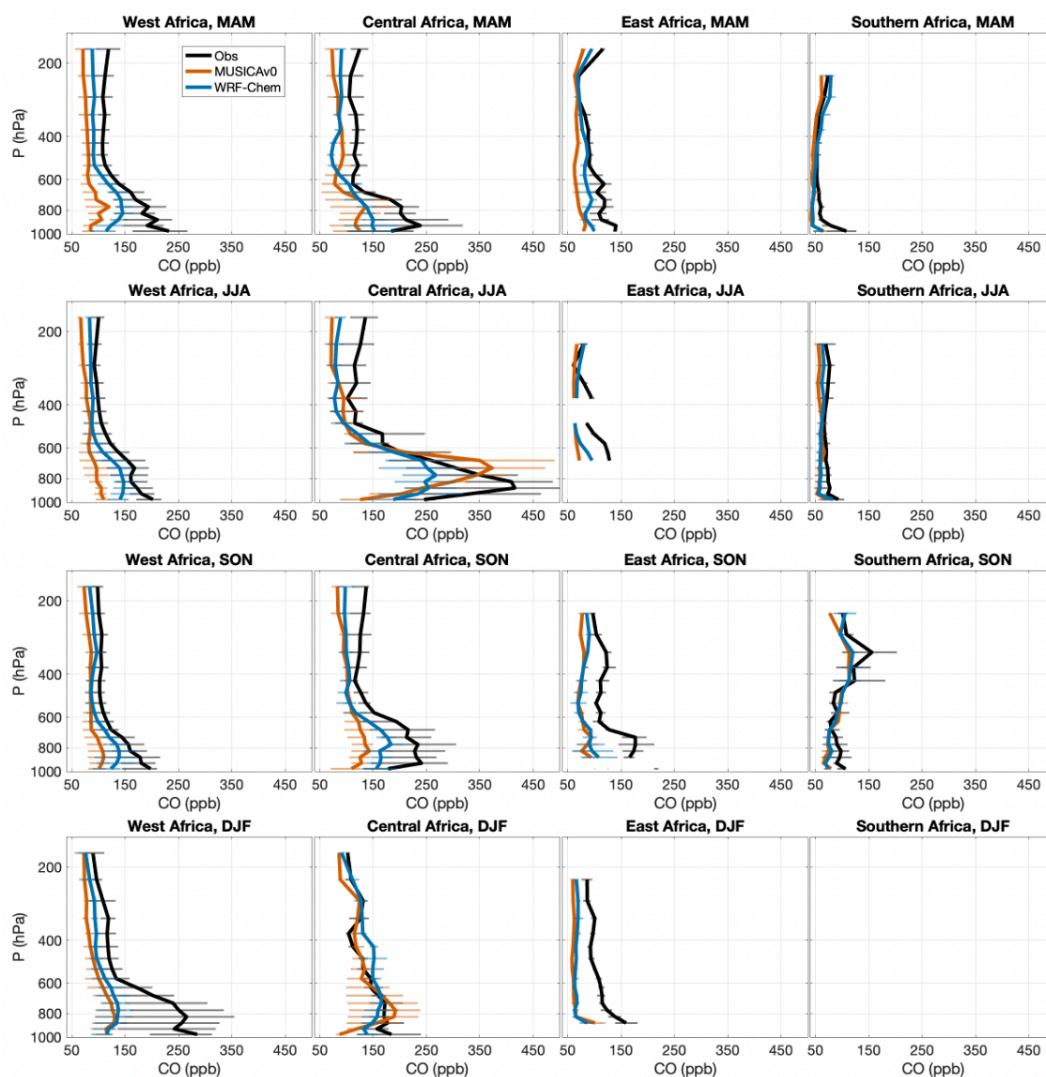


966
 967
 968
 969
 970
 971
 972

Figure 5. Monthly mean CO (ppb) from in situ observations (black), MUSICA v0 (red), and WRF-Chem (blue) during 2017 at (a) Assekrem, (b) Cape Point, (c) Izana, (d) Gobabeb, (e) Mare and (f) Ascension (see Figure 1b for locations). Monthly means are calculated from 3-hourly data. The range for each data point shows the variation of the 3-hourly data on that day (25% quantile to 75% quantile). Observational data are from World Data Centre for Greenhouse Gases (WDCGG).

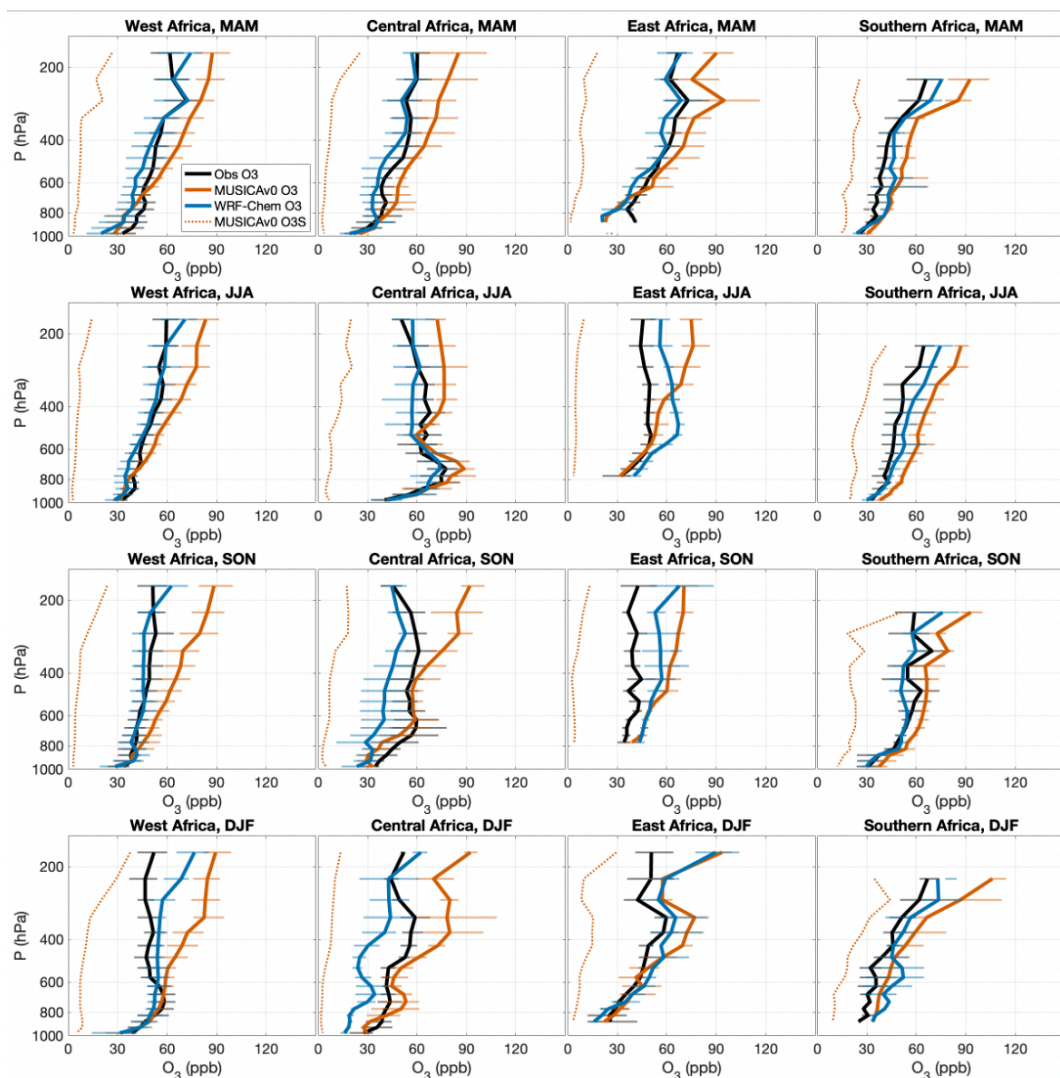


973
974

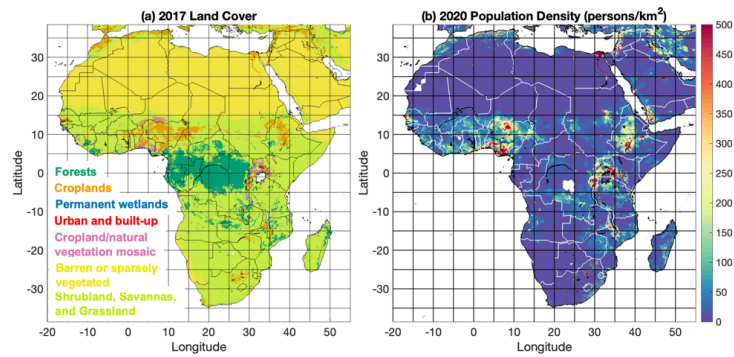


975
976
977
978
979
980
981
982
983

Figure 6. Vertical profiles of CO (ppb) from the In-service Aircraft for a Global Observing System (IAGOS) measurements (black) and corresponding model output from MUSICA v0 (red), and WRF-Chem (blue) during different seasons in 2017 over West Africa, Central Africa, East Africa, and Southern Africa. North Africa is not shown due to data availability. Seasonal mean profiles with the variation of the data in the pressure layer (25% quantile to 75% quantile) in MAM (March, April, and May), JJA (June, July, and August), SON (September, October, and November), and DJF (December, January, and February) are shown.

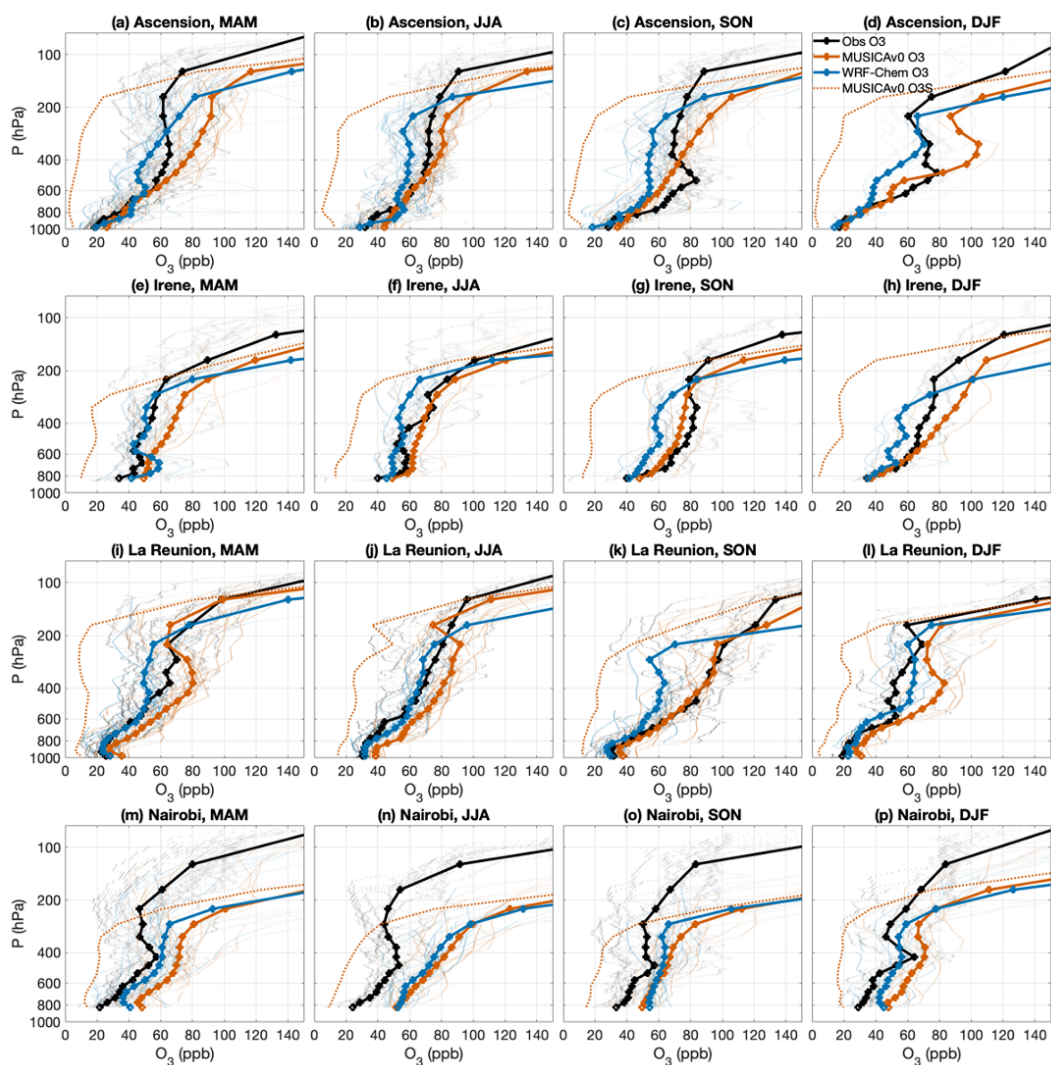


984
985 **Figure 7.** Vertical profiles of O₃ (ppb) from the In-service Aircraft for a Global Observing System
986 (IAGOS) measurements (black) and corresponding model output from MUSICAv0 (red), and
987 WRF-Chem (blue) during different seasons in 2017 over West Africa, Central Africa, East Africa,
988 and Southern Africa. North Africa is not shown due to data availability Seasonal mean profiles
989 with the variation of the data in the pressure layer (25% quantile to 75% quantile) in MAM (March,
990 April, and May), JJA (June, July, and August), SON (September, October, and November), and
991 DJF (December, January, and February) are shown. The dash red lines represent O3S
992 (stratospheric ozone tracer) from the MUSICAv0 simulation.

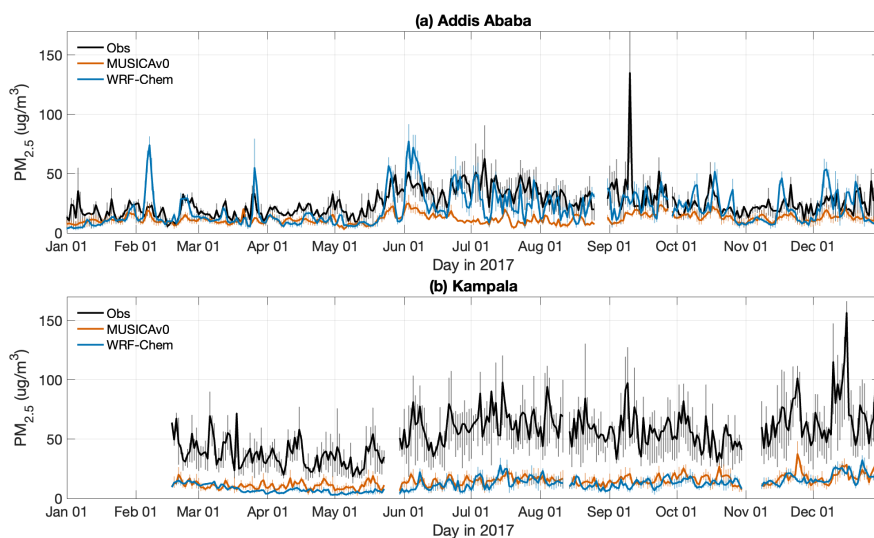


993
994 **Figure 8.** (a) Land cover in 2017 and (b) population density (persons/km²) in 2020 over Africa.
995 Land cover data is from MODIS/Terra+Aqua Land Cover Type Yearly L3 Global product
996 (resolution: 0.05 degree) (Friedl et al., 2022). Cropland/Natural Vegetation Mosaics means
997 Mosaics of small-scale cultivation (40-60%) with natural tree, shrub, or herbaceous vegetation.
998 Population density data is from the Gridded Population of the World, Version 4 (GPWv4),
999 Revision 11 (CIESIN, 2018).

1000
1001

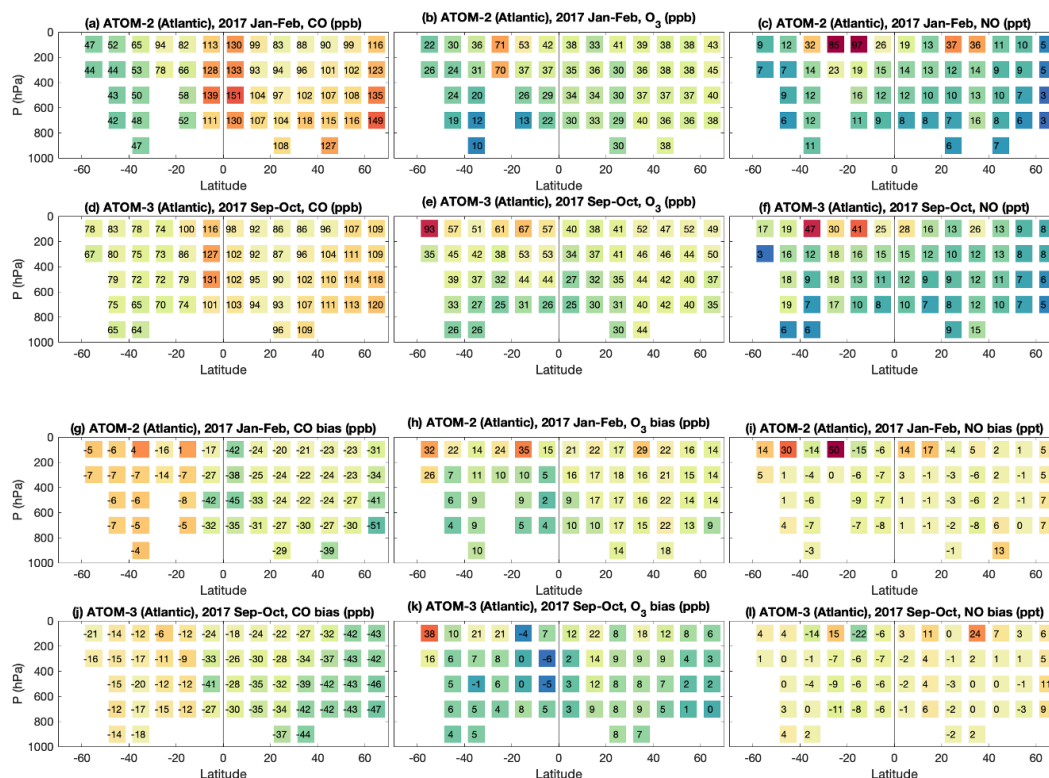


1002
1003 **Figure 9.** Vertical profiles of O₃ (ppb) from Ozonesondes (black) and corresponding model output
1004 from MUSICA v0 (red), and WRF-Chem (blue) for each season of 2017. The thick lines denote
1005 the seasonal mean profiles and the thin lines denote the individual profiles. The dash red lines
1006 represent O₃S (stratospheric ozone tracer) from the MUSICA v0 simulation. Ozonesonde data at
1007 Ascension in (a) MAM (March, April, and May), (b) JJA (June, July, and August), (c) SON
1008 (September, October, and November), and (d) DJF (December, January, and February) are shown.
1009 (e-h), (i-l), and (m-p) are the same as (a-d), except for Irene, La Reunion, and Nairobi, respectively.
1010 Locations of the sites are shown in Figure 1b.
1011

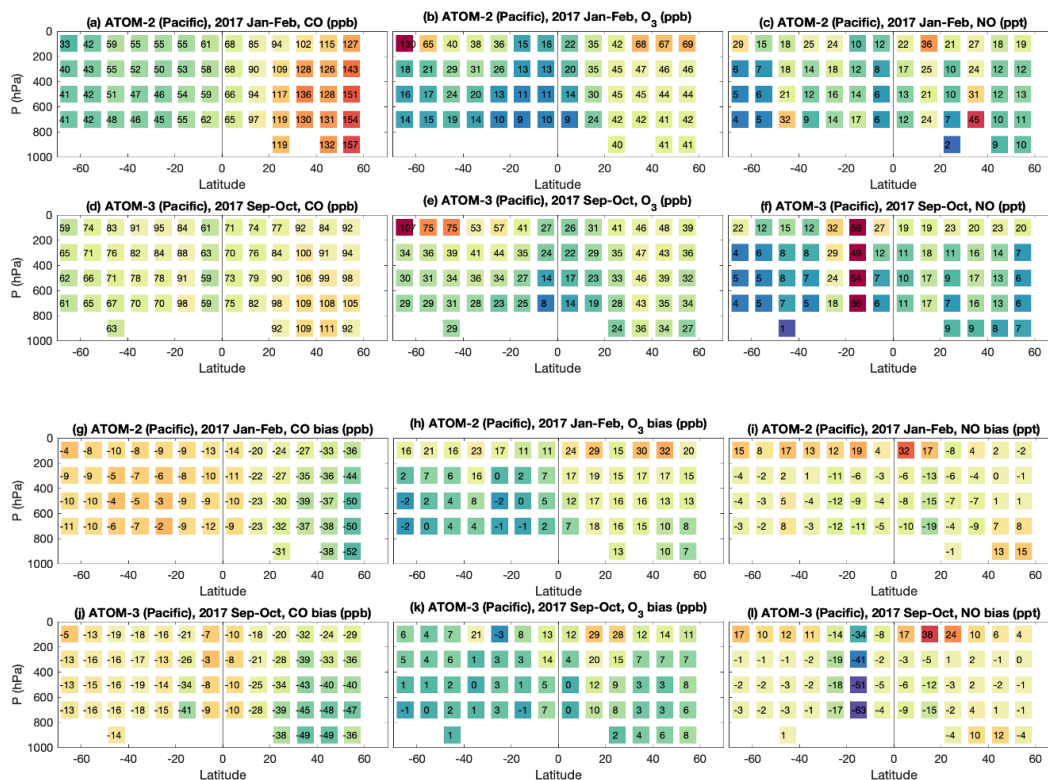


1012
1013
1014
1015
1016
1017
1018

Figure 10. Daily mean $PM_{2.5}$ from in situ observations (black), MUSICAv0 (red), and WRF-Chem (blue) during 2017 at (a) Addis Ababa and (b) Kampala. Daily means are calculated from 3-hourly data. The shown range for each data point shows the variation on that day (25% quantile to 75% quantile). Locations of the sites are shown in Figure 1b.

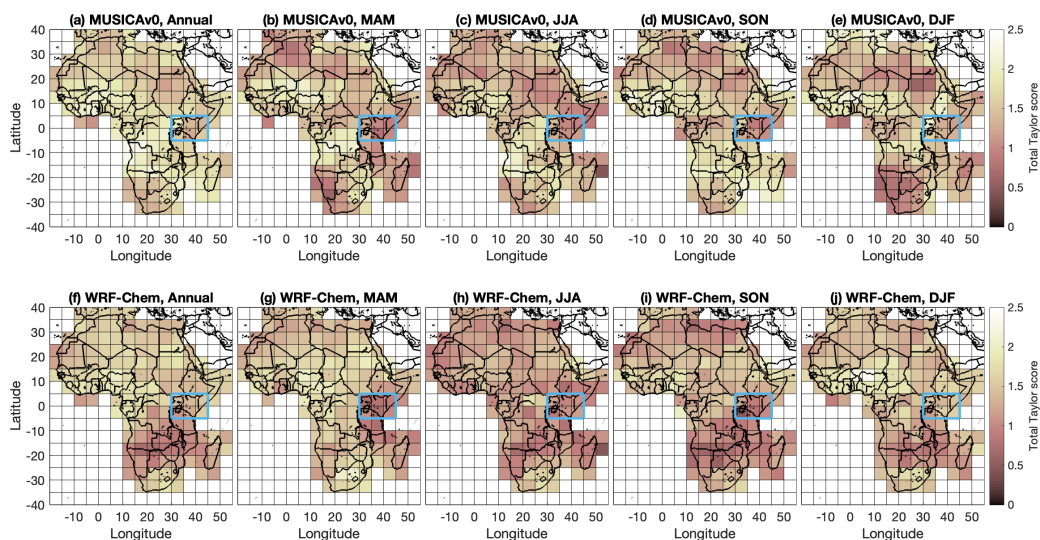


1019
 1020 **Figure 11.** Observations of (a) CO (ppb), (b) O₃ (ppb), and (c) NO (ppt) over Atlantic Ocean
 1021 during ATom-2 and ATom-3 (d-f). (g-l) corresponding model biases against ATOM observations.
 1022 The ATom airborne measurements and corresponding MUSICA_{v0} model results are binned to 10-
 1023 degree latitude and 200-hPa pressure bins. The values of mean biases for each latitude and
 1024 pressure bin are labeled in the figure.
 1025



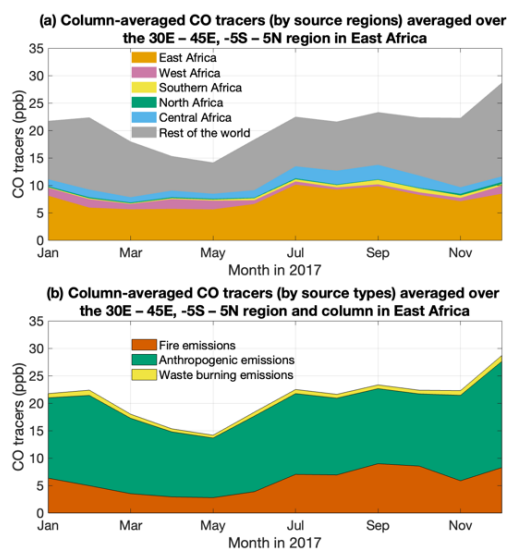
1026
 1027
 1028
 1029
 1030
 1031

Figure 12. Same as Figure 9 but for over the Pacific Ocean.



1032
1033
1034
1035
1036
1037
1038
1039
1040
1041
1042
1043
1044
1045

Figure 13. Spatial distribution of total Taylor score of MUSICA v0 and (f-j) WRF-Chem compared to satellite retrievals. In each $5^\circ \times 5^\circ$ (latitude \times longitude) pixel, Taylor scores of the model compared to three satellite products (e.g., MOPITT CO column retrievals, OMI tropospheric NO₂ column retrievals, and MODIS AOD) are calculated separately (as shown in Figure S8). Taylor score against each satellite product ranges from 0 to 1. And then three Taylor scores are summed up to obtain the shown total Taylor score (ranges from 0 to 3). Total Taylor score of MUSICA v0 for (a) 2017, (b) MAM (March, April, and May), (c) JJA (June, July, and August), (d) SON (September, October, and November), and (e) DJF (December, January, and February) are shown. The blue box highlights a potential region for future field campaigns and/or in situ observations. (f-j) are similar to (a-e) except for WRF-Chem.



1046
1047 **Figure 14.** Monthly time series of column-averaged CO tracers in the 30°E – 45°E, -5°S – 5°N
1048 region in East Africa. (a) CO tracers of emissions from North Africa (green), West Africa (pink),
1049 East Africa (orange), Central Africa (blue), Southern Africa (yellow), and the rest of the world
1050 (grey). (b) CO tracers of fire emissions (red), anthropogenic emissions (green), and waste burning
1051 emissions (yellow).

1052